JGR Atmospheres

RESEARCH ARTICLE
10.1029/2022JD037340

Key Points:

- The radiative flux profile data product (called ISCCP-FH) is described. It benefits from the new ISCCP cloud products (called ISCCP-H)
- The product is evaluated against the Clouds and the Earth's Radiant Energy System and the Baseline Surface Radiation Network measurements
- The long-term variations of top-of-atmosphere, surface and in-atmosphere net fluxes are documented and a possible cloud feedback is investigated

Correspondence to:
Y. Zhang,
yz7@columbia.edu

Citation:
Zhang, Y., & Rossow, W. B. (2023). Global radiative flux profile data set: Revised and extended. *Journal of Geophysical Research: Atmospheres*, *128*, e2022JD037340. https://doi.org/10.1029/2022JD037340

Received 19 JUN 2022
Accepted 11 FEB 2023

Author Contributions:
Conceptualization: Yuanchong Zhang, William B. Rossow
Data curation: Yuanchong Zhang, William B. Rossow
Formal analysis: Yuanchong Zhang, William B. Rossow
Funding acquisition: Yuanchong Zhang, William B. Rossow
Investigation: Yuanchong Zhang, William B. Rossow
Methodology: Yuanchong Zhang, William B. Rossow
Resources: Yuanchong Zhang, William B. Rossow
Software: Yuanchong Zhang
Validation: Yuanchong Zhang, William B. Rossow
Writing – original draft: William B. Rossow
Writing – review & editing: Yuanchong Zhang, William B. Rossow

Global Radiative Flux Profile Data Set: Revised and Extended

Yuanchong Zhang[1,2] **and William B. Rossow**[3]

[1]Business Integra, Inc., New York, NY, USA, [2]NASA Goddard Institute for Space Studies, New York, NY, USA, [3]Franklin, New York, USA

Abstract The third generation of the radiative flux profile data product, called ISCCP-FH, is described. The revisions over the previous generation (called ISCCP-FD) include improvements in the radiative model representation of gaseous and aerosol effects, as well as a refined statistical model of cloud vertical layer variations with cloud types, and increased spatial resolution. The new product benefits from the changes in the new H-version of the ISCCP cloud products (called ISCCP-H): higher spatial resolution, revised radiance calibration and treatment of ice clouds, treatment of aerosol effects, and revision of all the ancillary atmosphere and surface property products. The ISCCP-FH product is evaluated against more direct measurements from the Clouds and the Earth's Radiant Energy System and the Baseline Surface Radiation Network products, showing some small, overall reductions in average flux uncertainties; but the main results are similar to ISCCP-FD: the ISCCP-FH uncertainties remain $\lesssim$10 Wm^{-2} at the top-of-atmosphere (TOA) and $\lesssim$15 Wm^{-2} at surface for monthly, regional averages. The long-term variations of TOA, surface and in-atmosphere net fluxes are documented and the possible transient cloud feedback implications of a long-term change of clouds are investigated. The cloud and flux variations from 1998 to 2012 suggest a positive cloud-radiative feedback on the oceanic circulation and a negative feedback on the atmospheric circulation. This example demonstrates that the ISCCP-FH product can provide useful diagnostic information about weather-to-interannual scale variations of radiation induced by changes in cloudiness as well as atmospheric and surface properties.

Plain Language Summary The article describes the updated version of the International Satellite Cloud Climatology Project (ISCCP) radiative profile flux product, ISCCP-FH. This version has several important improvements over its previous two versions in its radiation model and input data sets of clouds, aerosol and other atmospheric and surface physical properties as well as ancillary data sets. Its spatial resolution is increased to 110 km. It now has uncertainties $\lesssim$10 Wm^{-2} at the top-of-atmosphere (TOA) and $\lesssim$15 Wm^{-2} at surface for monthly, regional averages based on validations against the direct observations at TOA and surface, slightly improved over the previous versions. We also describe long-term variations of the radiative energy intensity based on the product and give an example to study cloud-radiation feedback using this product. We expect the new product to be used in climate studies like its previous versions.

1. Introduction

Earth's climate is determined by a long-term, global balance of energy exchanges in the form of radiative fluxes, water phase changes, surface-atmosphere exchanges, and transports by the oceanic and atmospheric circulations; but the circulations and their transports are modified by the short-term, local imbalances of the energy and water exchanges. The atmospheric circulations (weather) produce water phase changes in the form of clouds and precipitation that feedback on all of these exchanges and circulation transports. The early focus of weather studies was on the precipitation produced from clouds. The early focus of climate studies was on the modulation of the top-of-atmosphere (TOA) radiative fluxes by cloud variations, usually the global average changes that are associated with global mean surface temperature changes. However the global mean temperature is not simply related to the average energy balance because changes in the atmospheric and oceanic circulation redistribute the energy, complicated by induced cloud feedbacks on these circulations. Hence, fully diagnosing cloud-radiative feedbacks on weather and climate requires decomposing the space-time variations of TOA fluxes into surface (SRF) net fluxes that affect the ocean circulation and atmospheric (ATM) net flux profiles that affect the atmospheric motions and cloud (and precipitation) formation. Since the solar (shortwave (SW)) fluxes act primarily on the surface and the terrestrial (longwave (LW)) fluxes act primarily on the atmosphere, these have to be diagnosed separately. This diagnosis has to be done across a range of space-time scales to establish the coupling at different scales of atmosphere-ocean motions.

Obtaining global observations that directly resolve bulk-cloud-process-scale variations of surface fluxes and atmospheric profiles of radiation is infeasible, so another approach is to measure the space-time-resolved variations of the properties of the clouds, atmosphere and the surface and then calculate the radiative fluxes with a detailed radiative transfer model. Atmospheric radiative transfer is sufficiently advanced that the accuracy of such calculations is primarily limited by the accuracy and completeness of the description of the cloud, atmosphere and surface properties input to the model. The knowledge and accuracy of this information has increased over the past few decades so that such calculations can improve to reliably reveal more detailed radiative exchanges and their variations. The advantage of the flux-calculation analysis is that determining the causes of flux variations is direct. The success of this approach depends on assessment of the accuracy of the input quantities against independent measurements and verification of the output fluxes against direct measurements.

This paper summarizes continuing work along these lines by describing a new data product, called ISCCP-FH, providing radiative flux profiles at 1°-equivalent-equal-area (approximately 110 km), 3-hr intervals, covering the whole globe for 35 years (see details in Y.-C. Zhang (2017)). This product is a revision of previous versions based on earlier International Satellite Cloud Climatology Project (ISCCP) data products (Rossow & Zhang, 1995; Y.-C. Zhang et al., 1995; Y.-C. Zhang et al., 2004). The new flux profiles are based on the new ISCCP-H cloud and atmosphere products (Rossow et al., 2022; Young et al., 2018) using a revised radiative transfer model with a refined statistical model of cloud vertical structure. The changes to the radiative transfer model and the input data are described in Sections 2 and 3, respectively. The resulting products are described and evaluated compared with more direct measurements of surface and TOA fluxes in Section 4. Some basic results and the long-term variations in the fluxes, especially the partitioning of the TOA fluxes into surface (SRF) and atmosphere (ATM) net fluxes and their average latitude variations, are summarized in Section 5. Section 6 discusses some possible implications for cloud-radiative feedbacks on atmosphere-ocean circulations of one example of cloud-induced changes in the net flux distributions. In conclusion Section 7 considers the state-of-art and suggests other diagnostic studies that can be done with this data product.

2. Changes in the Radiative Model

The radiative transfer model used for FH is a further revision of the model used for the two previous versions (FC and FD) and is equivalent to the current radiation code of ModelE2.1 of the NASA Goddard Institute for Space Studies (GISS) climate model (Kelly et al., 2020). Details of the model's physics are summarized in Y.-C. Zhang (2017), but an even more detailed description is in Y.-C. Zhang et al. (2004), especially Table 2. Basic features are (a) use of the correlated-k distribution to integrate over wavelength accounting for absorption and scattering in a vertically inhomogeneous atmosphere, (b) use of a single-Gauss point representation of the angular dependence of radiation, especially of solar radiation, (c) detailed microphysical and optical models of liquid and ice clouds as well as a variety of aerosols, (d) a treatment of the effects of small scale spatial inhomogeneity of clouds, (e) adjustable model levels to coincide with cloud top and bottom boundaries, where physically thicker clouds are divided into smaller layers, (f) spectrally dependent surface albedo and infrared emissivity by surface type, and (g) an angle-dependent ocean reflectivity model that accounts for wind-driven foam. The only revisions of the radiative transfer model for calculating the flux profiles from the previous version (see Y.-C. Zhang et al., 2004 for details) are: (a) reformulation of the SW line absorption for H_2O, O_2, CO_2, CH_4, N_2O, etc., using the HITRAN2012 atlas (Rothman et al., 2013) with added weak-SW-absorption values for H_2O, O_2, and CO_2 to eliminate an underestimate of atmospheric gas absorption (Oreopoulos et al., 2012), (b) improved LW modeling of the H_2O continuum, cloud flux change absorption cross-sections, SO_2 line absorption, and CH_4 and N_2O overlap, especially in polar conditions, (c) refined LW treatment for large water vapor amounts (e.g., DeAngelis et al., 2015), including accounting for within-layer water vapor gradients, and (d) increased base number of vertical layers from 24 to 43 for LW flux calculation. The code has an estimated accuracy of 1 Wm^{-2} for net LW fluxes throughout the troposphere and most of the stratosphere and close to 1% for SW fluxes as compared with line-by-line calculations (cf. Lacis & Oinas, 1991). For ISCCP-FH production, the monthly mean aerosol data in the model is replaced by the MAC-v2 global data set over all years (Kinne, 2019) for better treatment of the spectral details of stratospheric and tropospheric aerosol scattering and absorption and for consistency with the ISCCP-H cloud and surface retrievals (see Y.-C. Zhang et al., 2010, for sensitivity study of the effect of aerosol uncertainties on surface SW fluxes). Daily total solar irradiance (TSI) is changed to the Solar Radiation and Climate Experiment (V-15) based data set, which is equivalent to that used in the Clouds and the Earth's Radiant Energy System (CERES) products. Other changes of input parameters are based on the ISCCP-H data product

as described in the next section. The FH horizontal resolution is increased from FD to 1°-equivalent-equal-area (approximately 110 km scale) for consistency with the ISCCP-H cloud and ancillary data products. Features of the FH flux calculations that remain unchanged from the FD version (Y.-C. Zhang et al., 2004) are not considered here.

3. Changes in Input Data Set

Notable changes to produce ISCCP-H (Rossow, 2017; Rossow et al., 2022; Young et al., 2018), now covering 1983–2018, are: (a) refinements of cloud microphysical models, (b) introduction in the retrieval of finite cloud layer thicknesses that increase from the surface to the tropopause, (c) change of the ratio of ice and liquid cloud amounts from 0.96 to 0.64 by lowering the threshold temperature to 253 K, (d) a reduction of total cloud amount (CA) over high topography ice sheets in summer by about 0.10 (the only significant change) with a shift to more cirrus over both poles (polar cloud changes and evaluations are specifically discussed in Rossow et al., 2022), (e) placement of very thin cirrus at the tropopause instead above it, (f) treatment of stratospheric and tropospheric aerosol radiative effects in the cloud and surface retrievals, (g) treatment of surface temperature inversions and retrieval of physical surface temperatures (with correction of extreme values), and (h) 1°-equivalent-equal-area mapping of satellite pixels (∼5 km) sampled at 10 km intervals. Unlike ISCCP-D, ISCCP-H reports the interpolated amounts of the 18 cloud types (defined by top pressure, optical thickness and phase) over nighttime periods (except in winter polar regions). However, as with the FD products, the FH calculations need the full day and night time cloud properties of all the types (top temperature, optical thickness) in addition to their amounts. For most locations, the interpolation is between the nearest in time of before and after daytime results for each nighttime interval. For some locations where there is missing data and for the winter polar regions, the filling involves monthly diurnal averages from 3 years of data centered on each particular year, supplemented by long-term climatology (see Figure 1a in Y.-C. Zhang, 2017). The filling procedure provides complete cloud type properties over the whole global, every 3 hr.

All new ancillary inputs for FH (land-water mask, topography, sea ice and snow cover, total ozone abundance, stratospheric and tropospheric aerosol properties, atmospheric profiles of temperature and relative humidity) come from ISCCP-H on the same map grid (Young et al., 2018). These data sets have higher space-time resolutions than before and are more homogeneous over their records (see evaluations of the accuracy of the new ancillary products in Rossow, 2017). In particular, the atmospheric data set (called NNHIIRS) provides global 3-hr temperature-relative humidity profiles at 16 atmospheric levels with surface temperature inversions.

Gas abundances (except for water vapor and ozone) are specified as in the GISS climate model, including positive trends in CO_2 and CH_4 abundances from observations (e.g., Hansen et al., 1988; the most up-to-date trends can be found in "Forcings in GISS Climate Model" at https://data.giss.nasa.gov/modelforce/ghgases/). Surface albedos (except for water) are derived from an aerosol-corrected surface visible reflectance from ISCCP-H and a 6-band spectral dependence model (following Y.-C. Zhang et al., 2004, 2007) for different surface types (although the surface reflectances in ISCCP-H in the visible have been corrected for stratospheric and tropospheric aerosol scattering/absorption using MAC-v1, Kinne et al., 2013, the adjustment in FH is done using the full spectral dependence of a later version of the aerosol product, MAC-v2, Kinne, 2019). Surface temperatures from ISCCP-H are physical values obtained using estimated narrowband emissivities (at ∼11 μm wavelength) by surface type (Rossow, 2017); broadband emissivities by surface type are used in FH calculations (Y.-C. Zhang et al., 2007). The diurnal variations of surface air and skin temperatures from ISCCP-H (which are clear-sky biased) are corrected for cloud effects (Y. Zhang et al., 2006).

A cloud vertical layer (CVL) model accounts for cloud layer overlap in our profile calculations by assigning specific layer structures to each of the ISCCP cloud types that are defined by three intervals of cloud top pressure, three intervals of optical thickness and phase (including interpolated values over nighttime and in winter polar conditions). In each map cell at each time, radiative flux profiles are calculated for each individual layer structure that is present, as well as clear sky (even when not present), and then these are averaged with area-fraction weights to give one flux profile. The original CVL model (Rossow et al., 2005), used for FD (Y.-C. Zhang et al., 2004, Table 5), was based on ISCCP-D and a cloud layer climatology derived from radiosonde humidity profiles (Wang et al., 2000) and later evaluated against CloudSat-CALIPSO profiles (Rossow & Zhang, 2010). Table 3 in Rossow and Zhang (2010) showed excellent statistical agreement between that model and the radar-lidar profiles and Figures 5 and 6 in that paper show the mean latitude dependence of cloud profiles over ocean and land. The one

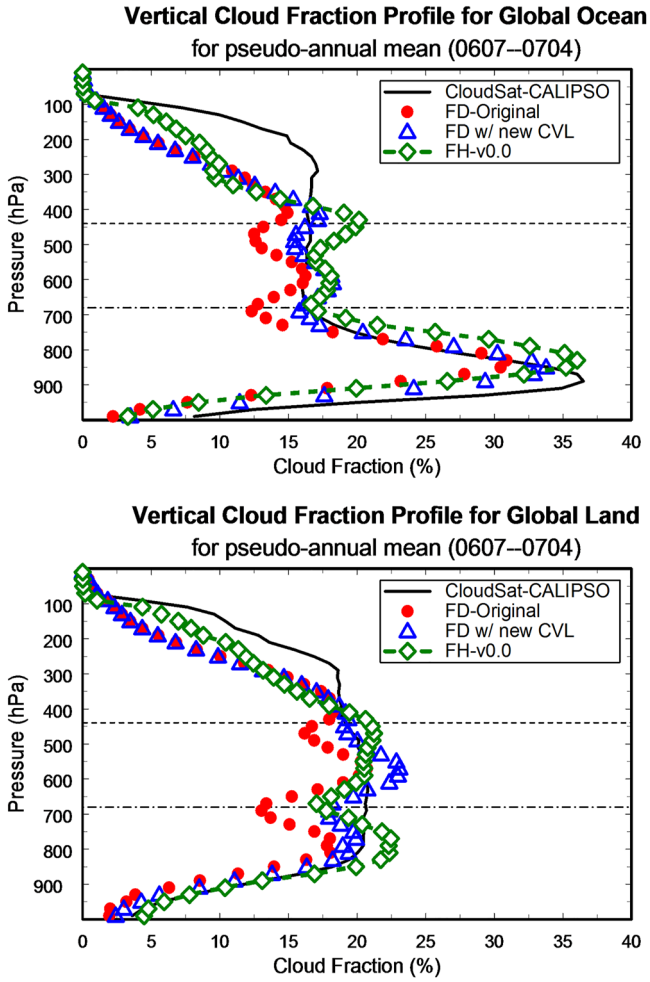

Figure 1. Global mean cloud amounts (%) at each pressure (hPa) averaged over four mid-season months in 2007 (pseudo-annual mean) over ocean (upper panel) and land (lower panel) from CloudSat-CALIPSO (solid black line), the original profile used for ISCCP-FD (red dots), the profile produced by the refined cloud vertical layer model (CVL) applied to ISCCP-D cloudiness (blue triangles), and applied to ISCCP-H cloudiness (green diamonds) as used in ISCCP-FH. The horizontal dashed black lines indicate the pressure boundaries separating low, middle and high cloud tops.

notable discrepancy was that there was much more single-layer low cloud in that version of CloudSat-CALISPO that was identified by ISCCP-D as clear sky, but this discrepancy was much reduced in a later version of the lidar analysis that resolved confusion between aerosols and cloud (Mace & Zhang, 2014). Although the assignment of layer structures to the ISCCP cloud types remains the same for FH as in FD, the resulting vertical distribution is slightly changed by revision of the layer position for obscured clouds and the thickness climatology (varying by cloud optical thickness, latitude/longitude, month-of-year, ocean/land) based on CloudSat-CALIPSO 2B-GEOPROF-LIDAR (P2_R04, henceforth RL-GEOPROF).

The refined statistical CVL model used in FH is illustrated in Figure 1 compared with the older model and with RL-GEOPROF (P2_R04 – this is the 1/3 km lidar version). This version of GeoProf uses Version 3 of the CALIPSO products that made significant changes in the amount of low cloud relative to the earlier version (Mace & Zhang, 2014); however Version 4 of CALIPSO makes more changes, including in the amount of upper troposphere cloud (Liu et al., 2019). Also shown is the refined CVL model applied to ISCCP-D clouds. Although the FH CVL model makes adjustments of the ISCCP cloud distribution (see Y.-C. Zhang et al., 2004) to increase low CA to account for higher-layer-obscuration and to increase thin high-level CA to account for misplacement of some of these clouds to lower levels, the new result still underestimates CA at the highest levels in general by about 0.05–0.10. Some of the underestimate of high CA is caused by missed detections of very thin clouds (C. Stubenrauch et al., 2012, C. J. Stubenrauch et al., 2013), some by misplacement of thin clouds overlapping lower level clouds (Jin & Rossow, 1997) and some by the fact that the radiative tops for clouds, especially in the tropics, appears lower than the physical top (Liao et al., 1995). The latter two effects may explain the small excess of CA near the 440 hPa level shown in Figure 1. Low CA over ocean for FH agrees well with RL-GEOPROF but is overestimated by about 0.03 over land (given the small changes in the CVL, Figures 5 and 6 in Rossow & Zhang, 2010, still show the zonal monthly mean vertical distribution). The continued refinement of the CloudSat and CALIPSO products (Liu et al., 2019; Mace & Zhang, 2014; Protat et al., 2014) makes the magnitude of these differences uncertain. (At the time of writing, the "active release versions for 2B-GEOPROF-LIDAR are R04 & R05; P1_R05 is the current version and R04 products will be available until all R05 products have been released," see https://www.cloudsat.cira.colostate.edu/data-products/2b-geoprof-lidar).

4. Product Description and Evaluation

The FH products report the upward and downward SW and LW fluxes at five levels from the surface to the TOA for "full" sky (actual variable cloud cover), clear sky and overcast sky, as well as the diffuse and direct SW fluxes at the surface. These results are compiled in five sub-products (all in NetCDF except the last): FH-TOA (radiative fluxes at TOA with relevant physical quantities, 23 variables), FH-SRF (radiative fluxes at surface with relevant physical quantities, 34 variables), FH-PRF (fluxes at the surface, 680, 440, 100 hPa, TOA at about 100 km altitude, 91 variables), FH-MPF (monthly average of FH-PRF) and FH-INP (complete inputs up to 355 variables). All of these products are mapped at 1°-equivalent-equal-area and all, except MPF, are reported at 3-hr intervals.

Extensive comparisons of the previous versions of this product are the foundation for documenting the small changes/improvements made to the ISCCP-FH products (Rossow & Zhang, 1995; Y.-C. Zhang et al., 1995; Y.-C. Zhang et al., 2004; Y. Zhang et al., 2006; Y.-C. Zhang et al., 2007; as well as Raschke et al., 2012, 2016). Y.-C. Zhang et al. (1995) conducted a complete set of sensitivity studies to determine how uncertainties in the inputs translate to flux uncertainties (still valid for FH), emphasizing the leading importance of clouds for

Table 1
Differences of Monthly Mean ISCCP-FH and FD TOA Fluxes With CERES (Edition 3A, CERES Science Team, 2013) and Surface Fluxes With Baseline Surface Radiation Network Stations (Ohmura et al., 1998) in Wm^{-2} for 2007

TOA		
	FH minus CERES	FD minus CERES
SWnet	−7 ± 6	−8 ± 6
Correlation for SWnet	0.99	0.99
LWnet	+7 ± 3	+3 ± 3
Correlation for LWnet	0.99	0.99
Overall uncertainty	≤10	≤10
Surface		
	FH minus BSRN	FD minus BSRN
SWnet	−1 ± 15	−4 ± 17
Correlation for SWnet	0.99	0.99
LWnet	−7 ± 12	+10 ± 14
Correlation for LWnet	0.97	0.97
Overall uncertainty	≤15	≤20

Note. The statistics include spatial variability over location at 110 km scale as well as month-to-month variability. The uncertainty range is based on the normal deviations (rms with bias removed) (cf. Rossow & Zhang, 1995).

SW fluxes and atmospheric and surface temperatures for LW fluxes. Rossow and Zhang (1995) highlighted the dominance on small space-time scales of sampling differences in comparisons of the calculated fluxes with direct measurements, but also showed that differences in monthly averages better indicated biases in inputs to the calculations. Rossow and Zhang (1995) also conducted a detailed set of comparisons with direct TOA and SRF flux measurements, investigating in particular the effects of differences in space-time sampling and coverage in such comparisons. The mismatch of spatial scales exaggerates the differences for surface flux comparisons by 30%–100% because the meteorological conditions do not always match (Rossow & Zhang, 1995; Y.-C. Zhang et al., 2010). The better matching of satellite products contributes less uncertainty. Y.-C. Zhang et al. (2010) also examined the effects of errors in aerosol optical depth on the FD-calculated downwelling SW (SWdn) fluxes, motivating the change in the aerosol data set used for FH. More detailed evaluations of the input quantities, other than clouds, were conducted in Y. Zhang et al. (2006), Y.-C. Zhang et al. (2007), which served as the basis for improving the ancillary products, particularly the atmospheric temperature-humidity profiles. Evaluations of the new (non-cloud) inputs for FH are discussed in Rossow (2017) and Rossow et al. (2022). More general evaluations of the previous flux products, including mapped comparisons and time variations, were made in Rossow and Zhang (1995) and Y.-C. Zhang et al. (2004). Features of the calculations that remain unchanged from FD are not considered here.

A summary estimate of the uncertainties of FH and FD fluxes is shown in Table 1 based on monthly mean comparisons for 2007 at 1° mapping to CERES (SYN1deg Ed3A, see CERES Science Team, 2013) for TOA fluxes and collocated Baseline Surface Radiation Network stations (BSRN, Driemel et al., 2018; Ohmura et al., 1998) for SRF fluxes. Comparisons were also made by Stackhouse et al. (2021) to the latest version of GEWEX-SRB Rel4 (which is also based on ISCCP-H) with respect to CERES Energy Balanced and Filled (EBAF) Ed4.1 (Loeb et al., 2018), which is an adjusted version of Ed3A to reduce the original net imbalance of +4.3 Wm^{-2} to force agreement with an imbalance estimate of <1 Wm^{-2} from ocean heat measurements (Loeb et al., 2009). The comparison results from Stackhouse et al. (2021) to a later version of CERES do not indicate any changes of the comparison statistics for the overall biases (and standard deviation) shown in Table 1. Raschke et al. (2012, 2016) compare many of these same products, including ERBE, multiple versions of CERES, BSRN, as well as SRB and ISCCP-FD, in much more detail.

The comparison statistics (much more detail is given in Y.-C. Zhang (2017)) indicate that the FH results are only a very slight improvement over the FD results (Y.-C. Zhang et al., 2004). These statistics encompass both

Table 2
Evolution of Flux Biases (Wm^{-2}) From Comparisons With Spatially Matched ERBE or CERES at Top-Of-Atmosphere and the Global Energy Balance Archive (Wild et al., 2018) or BSRN at Surface (Driemel et al., 2018)[a]

TOA			
	FC—ERBE	FD—ERBE	FH—CERES
SWup	+10.7	+4.7	+7.2 (+7.5, +5.0)
LWup	−1.1	−2.2	−7.1 (−7.0, −8.0)
Net	−9.3	−2.0	0.0 (−0.5, −3.2)
Surface			
	FC—GEBA	FD—BSRN	FH—BSRN
SWdn	+15.2	+2.0	−1.4
LWdn	−19.4	+2.2	−7.5
Net	N/A	N/A	(+4.1)

[a]The FC comparisons are based on 16 seasonal months over 1985–1989 as reported in Rossow and Zhang (1995). The FD comparison with ERBE is also based on the same 16 seasonal months as FC but the FD comparison with BSRN is based on all months over 1992–2001 as reported in Y.-C. Zhang et al. (2004). The FH comparisons are based on monthly means in 2007 from CERES (SYN1deg Ed3a) and BSRN; values in parentheses represent the bias with respect to CERES SYN1deg 4.1 for 2007–2009 period and EBAF 4.1 over the 2001–2009 period, respectively, cited from Stackhouse et al. (2021).

spatial variation of monthly averages over the global (110 km scale) and month-to-month variations, seasons included. Clear sky SW absorption has increased producing better agreement with line-by-line calculations (cf. Oreopoulos et al., 2012). As noted below some changes in surface LW fluxes are associated with the change of atmospheric temperature-humidity inputs. The changes in ISCCP-H cloud microphysics did not produce notable changes in the fluxes overall. Although some notable changes of polar cloud properties occurred in ISCCP-H (decrease of total CA in southern summer with shift of some remaining clouds to cirrus category at both poles), the only significant change in the FH polar fluxes is a decrease of surface LWdn by 10%–20% (more in northern winter and southern summer). This decrease is caused almost entirely by the change of the ancillary atmospheric temperature-humidity data set from the operational Television Infrared Observation Satellite in FD to the new neural network High Resolution Infrared Radiation Sounder (NNHIRS) in FH. The latter is considerably colder (5–10 K) near the surface (but about the same at higher altitudes) than the former, which was based on a fixed climatology estimated from conventional observations made from 1958 to 1973. NNHIRS is more consistent with other temperature data (Rossow et al., 2022). All other differences of monthly mean fluxes between FD and FH in the polar regions are <10 Wm^{-2}.

The dominant source of uncertainty in the flux profiles is still associated with the cloud vertical layer (CVL) model, which is a small improvement over the previous version (Figure 1). The new model still underestimates cloud amounts near the tropopause (at the 200 hPa level) by about 0.05 (land) and 0.10 (ocean). Based on the GEWEX assessment of ISCCP-D clouds (C. J. Stubenrauch et al., 2013), some of these high clouds (about 0.05) are actually missed by ISCCP-D, but they have such low optical thicknesses that the resulting flux biases are estimated to be <1 Wm^{-2} (Y.-C. Zhang et al., 2004). Most of the near-tropopause clouds are actually detected but displaced to lower levels; as shown by T. Chen and Rossow (2002), even though these clouds are consistent with the narrow-band Infrared wavelength radiances, they are below the water vapor emission level at wavelengths >25 μm, which may account for part of an underestimate of LW emission (LWup) at TOA. The new cloud vertical model also overestimates low-level CA by about 0.03 over land but not ocean and top pressure for low clouds by about 75 hPa over oceans., Although Figure 1 shows an overestimate of low CA over land relative to RL-GEOPROF, the BSRN comparison still indicates a small low bias of LWdn at the surface in FH, associated with the change in atmospheric temperature-humidity profiles. The new product in ISCCP-H (NNHIRS) has near-surface air temperatures within 1–2 K over land compared to surface measurements but is drier at the surface over land (Rossow et al., 2022).

To estimate the effects on fluxes of uncertainties in the cloud layer amounts, flux profiles were calculated for the middle day of the four mid-season months (January, April, July, October 2007) with high cloud amounts (cirrus, cirrostratus, defined by optical thickness <23) increased or low cloud amounts (all types) decreased as Figure 1 suggests. Although the input cloud amounts from ISCCP-H were changed globally, the resulting changes at each

location and level are limited by the constraint that total CA cannot exceed unity nor can a type of cloud fraction become negative. Hence the global average changes are smaller than some local changes. Since the atmospheric absorption of solar radiation is weak, the SW flux profile is relatively insensitive to the vertical distribution of clouds, especially since the total optical thickness is constrained (cf. T. Chen et al., 2000). For an increase (decrease) of high (low) global mean CA of about 0.05, the global mean SWnet at all levels decreases (increases) by about 6–7 Wm^{-2}, with a slightly larger change near the surface for changing low CA and at mid-levels for changing high CA. Since the total optical thickness is constrained to be the same, most of this change occurs simply because total CA is increased (decreased). Thus uncertainties in the CVL of this magnitude, if constrained by total CA and optical thickness, contribute very little uncertainty in the shape of the SWnet profile (see also Y.-C. Zhang et al., 1995, for sensitivity tests of the effects of uncertainties in total CA and optical thickness). For similar changes in high (low) cloud amounts, the global mean LWnet (which is negative) increases by about 3–6 Wm^{-2} going from the surface to TOA for the high cloud increase and decreases by about 1–3 Wm^{-2} going from TOA to the surface for the low cloud decrease. Thus, although local effects can be larger, the uncertainty of net fluxes at all levels in the atmosphere is of the same order as the flux uncertainties at TOA and surface shown in Table 1: the total flux profile uncertainties, especially in LW, are larger because of uncertainties in the atmospheric temperature (and humidity) profile.

Table 2 shows the evolution of comparison differences for the three versions of these products (including alternate versions of the CERES products, cf. Stackhouse et al., 2021). The bias of FH upwelling SW (SWup) flux at TOA with respect to CERES is consistent in sign with the bias of SWdn flux at SRF with respect to BSRN, an improvement over the FC/FD SW biases that were not consistent at TOA and SRF. The bias of SWdn and LWdn at SRF is much smaller for FD and FH compared to BSRN than for FC compared to GEBA. The smaller bias of LWup at TOA in FC/FD when compared with the Earth Radiation Budget Experiment (ERBE) becomes larger for FH when compared to CERES, even though the latter flux is smaller than ERBE and the FH flux is smaller than FC/FD. These differences for FH are still within the uncertainties of the comparison data sets as discussed next.

The changing comparison results in Table 2 can also be related to changes in the data sets used for evaluation of FC/FD/FH that have their own uncertainties, including uncertainty in calibration, which is smaller for CERES/BSRN than for ERBE/GEBA. Thus, some of the changes (especially biases) in the comparison results could be caused by changed reference data. In addition, there are differences in the wavelength ranges defining SW and LW fluxes (measurements are corrected for limited instrument sensitivity), treatment of angle dependence (measurements are corrected) and domain area represented (smaller for surface measurements than satellite-based products).

ERBE/CERES separate SW and LW at 5.0 μm, calibrating to account for instrument sensitivity ranges that do not correspond precisely to this division. The ERBE scanners were sensitive in the (approximate) wavelength range of 0.2–4.5 μm in the SW and 6–35 μm in the LW; the ERBE LW is truncated at 50 μm (Barkstrom et al., 1989). The CERES instruments are sensitive in the range 0.3–5 μm in the SW and 5–200 μm in the LW (Loeb et al., 2018), which is determined from a Total channel (0.3–200 μm) with a decreasing sensitivity longward of 30 μm (Loeb et al., 2001). For surface SW instruments, corrections are needed for the dome transmission (estimated at about 0.95) and an uncertain thermal offset; LW instruments have various SW cutoffs at 3.5–5.0 μm to exclude sunlight, but there is some thermal radiation in this wavelength range (Kohsiek et al., 2006). Philipona et al. (2001) describe the typical wavelength coverage by SW instruments as 0.3–2.8 μm and LW as 4.0–50 μm, with as much as 2% of the LW flux at wavelengths >50 μm; they estimate the resultant flux uncertainties of SW ± 5 Wm^{-2} and LW ± 10 Wm^{-2}. FH (as well as FC/FD) includes wavelengths 0.2–15.0 μm in the SW radiation from the sun, but without thermal radiation from Earth, and includes wavelengths 0.2–200 μm in the LW radiation from Earth (for a complete Planck function), but without solar radiation. Effectively, however, the calculated fluxes represent 0.2–5.0 μm for SW and 5.0–200 μm for LW.

There could also be subtle differences in the treatment of angle dependencies of the direct measurements, which have to be corrected, and the radiative transfer calculations. The satellite radiance measurements are converted to fluxes using empirical angle dependence models that have different but much more detailed scene dependencies for CERES than for ERBE (Loeb et al., 2001; Su et al., 2015a, 2015b). The surface measurements have to be corrected for sensor angle dependence (e.g., Michalsky et al., 1999).

The satellite-based flux data products represent larger areas (of order 110 km in size for FH but about 280 km for FC/FD) than the surface measurements (of order 50 km in size), which introduce differences in the presence of incomplete cloud cover (cf. Rossow & Zhang, 1995). The radiative transfer calculations ignore small lateral exchanges (a better approximation at larger scales). Y.-C. Zhang et al. (2010) show that simple comparisons of the satellite-based products with surface measurements exhibit significantly larger differences if cloud

Table 3
(First Three Numerical Columns) Comparison of Global-Time-Average Flux Results for 16 Mid-Seasonal Months for the Same Four Year Period (April 1985–January 1989) From the Three Versions of Calculations (All Are in Wm^{-2} Except Albedo in %) and (Rightmost Column) Mean (Standard Deviation) of 1°-Equal-Area Maps Over All the Monthly Means From July 1983 to June 2017[a]

Quantity	FC	FD	FH	34-year FH
TOA				
SWdn	341.6	341.8	340.3	340.4 (130.9)
SWup	111.5	105.6	104.6	104.5 (50.6)
LWup	234.2	233.2	231.5	232.3 (32.8)
SWnet	230.1	236.3	235.7	236.1 (107.1)
LWnet	−234.2	−233.2	−231.5	−232.3 (32.8)
NET	−4.1	3.1	4.2	3.8 (88.3)
SWcre	−53.7	−50.4	−49.0	−48.8 (33.8)
LWcre	21.3	26.2	28.3	26.9 (15.4)
Albedo	32.6	30.9	30.7	30.7 (13.8)
Atmosphere				
SWnet	65.0	70.8	77.4	77.0 (30.5)
LWnet	−188.4	−182.0	−179.8	−178.9 (37.6)
NET	−123.4	−111.2	−102.5	−101.9 (33.2)
SWcre	−1.6	2.9	2.5	2.6 (3.5)
LWcre	−3.6	−3.1	7.1	5.4 (20.8)
Surface				
SWdn	193.4	189.4	183.4	183.9 (84.2)
SWup	28.3	24.0	25.1	24.8 (35.2)
LWdn	348.3	344.6	346.0	340.9 (76.1)
LWup	394.1	395.7	397.6	394.3 (75.6)
SWnet	165.1	165.4	158.3	159.1 (80.3)
LWnet	−45.8	−51.1	−51.6	−53.4 (25.7)
NET	119.3	114.3	106.7	105.7 (83.5)
SWcre	−52.2	−53.3	−51.5	−51.5 (36.0)
LWcre	24.9	29.3	21.2	21.5 (15.3)
Albedo	14.6	12.7	13.7	13.5 (18.6)

[a]Cloud Radiative Effect (CRE as used in this table in SWcre and LWcre for SW and LW, respectively) is for net fluxes, positive sign means radiative heating in the system (the earth-atmosphere, earth or atmosphere system for TOA, surface or atmosphere) as conventionally defined. The original FH 1°-equal-area map is re-gridded to the same 2.5°-equal-area map as FC and FD before averaging for the 16-month comparison, but not in the last column. Albedo for both TOA and SRF are calculated based on averaged SWup and SWdn (because albedo is the ratio of SWup to SWdn that cannot be linearly averaged); however, the standard deviation for Albedo is based on all monthly mean albedo values (like all other parameters) for a reference.

and atmospheric conditions are not matched: rms differences in SW fluxes decrease by a factor of about two if cloud cover and optical thickness agree and LW flux rms differences decrease by as much as 30% if cloud cover and atmospheric temperature are matched with biases almost eliminated.

Another systematic difference is that ERBE/CERES define the TOA to be at 30 and 20 km, respectively (Barkstrom et al., 1989 for ERBE, Loeb et al., 2018 for CERES), whereas FC/FD/FH define TOA at 100 km. In FH the average differences in upward fluxes between the 100 hPa level and TOA imply that the flux difference related to this difference in reference level is <1 Wm^{-2} for SW but could be as much as 2–3 Wm^{-2} for LW, which might be part of the lower FH values relative to ERBE/CERES (Table 2).

Given the uncertainties of the comparison data sets and the estimates for FH based on previous evaluations, especially the sensitivity tests for the input data sets, the overall uncertainty of the FH fluxes (including the profiles) is in the range between the TOA and surface estimates shown in Table 1, namely about 10–15 W/m^2 for monthly averages at 110 km scale.

Table 3 compares the flux results from all three versions as global mean values averaged over the same 5 year period (mid-seasonal months for April 1985–January 1989), including Cloud Radiative Effect (CRE, the difference between all-sky and clear-sky fluxes). The systematic decrease of SWup at TOA and SWdn at SRF, as well as increase of SWnet in ATM, from FC to FD is caused by the added treatment of ice clouds in FD; the changes from FD to FH reflect the addition of more atmospheric absorption mostly by gases and a little by aerosols. An increase of surface albedo between FD and FH is related to the added treatment of aerosols in ISCCP-H and a more detailed climatology in FH. The small decrease in LWup (and increase in LWcre) at TOA between FD and FH is related to small increases of high-level cloudiness (in FC only the average cloud top temperature over each map grid domain is used whereas FD and FH determine fluxes for a distribution of cloud properties within each domain). Despite the elimination of extreme surface temperatures in ISCCP-H (Rossow et al., 2022), SRF LWup increased slightly in FH compared with FD. Small changes in the treatment of low cloud base estimates in the CVL from FD to FH, as well as the changes in atmospheric temperature-humidity, caused a decrease of LWcre at SRF for FH. These small changes in the lower atmosphere clouds and temperature-humidity changed the sign of the small in-atmosphere LWcre in FH to a small heating effect. In general, however, the overall changes from FC to FH are relatively small, similar in magnitude to the estimated uncertainties. The last column in Table 3 summarizes the FH results averaged over 34 whole years (July 1983–June 2017), where the standard deviations include both the spatial variability of monthly mean values in the 1°-equivalent-equal-area mapping and the month-to-month variations, seasons included. The overall assessment of cloud radiative effects is that they reduce the heating of Earth at TOA by about 22 Wm^{-2}, which appears as a reduction of surface heating by about 30 Wm^{-2} but a heating of the atmosphere by 8 Wm^{-2} (cf. Table 2 in Wild et al., 2018).

5. Some Features of the Long-Term FH Record

Despite the magnitude of the estimated uncertainties of the monthly mean FH fluxes (Table 1), the long-term record of global mean net flux anomalies at TOA over about the last 15 years shows agreement within mutual uncertainties with the CERES (SYN1deg Ed4.1) record, especially in SWnet (Figure 2) (cf. EBAF Ed4.1 anomalies in Loeb et al. (2021)). This comparison

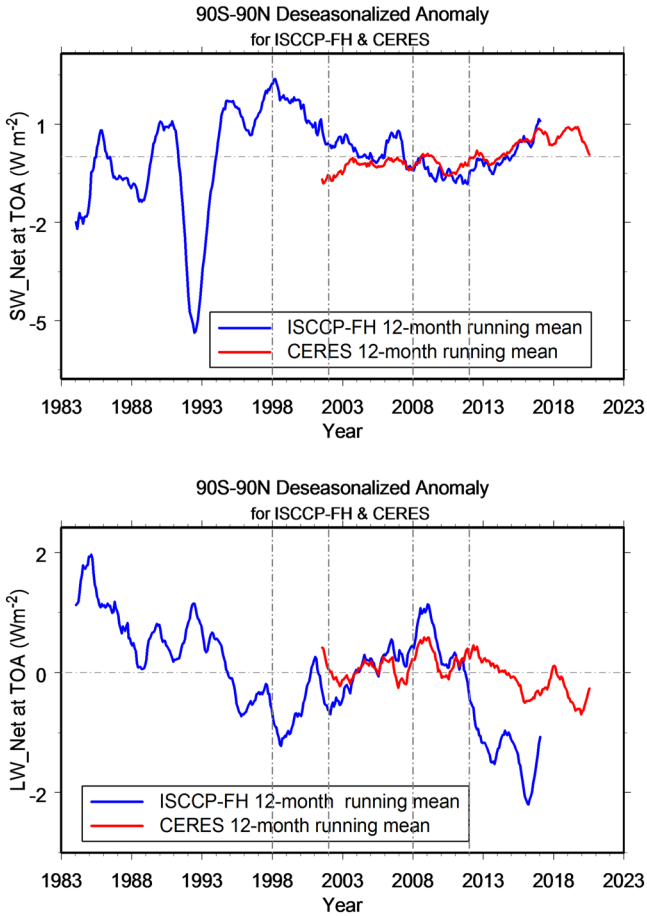

Figure 2. Deseasonalized anomalies (shown as 12-month running averages) of global monthly mean TOA net fluxes (Wm^{-2}) from FH (blue curves) compared to Clouds and the Earth's Radiant Energy System (CERES) (SYN1deg Ed4.1, red curves) for SWnet (upper panel) and LWnet (lower panel) from 1983 to 2019, where FH covers July 1983 to June 2017 while CERES covers 2001 to 2020. The anomalies for each data set are determined relative to their own record averages. Positive SWnet anomaly indicates more absorption (lower planetary albedo) and positive LWnet anomaly indicates decreased emission. The vertical lines delineate two time periods (1998–2002, 2008–2012) discussed later.

provides an additional evaluation of FH, especially since the anomalies shown are relative to each data sets own record average. The longer FH record suggests that the recent increase in SWnet (decreased albedo, see also Goode et al., 2021; Stephens et al., 2022) may not be a trend but a long-term variation. However, the magnitude of the recent changes in LWnet in FH (decreased emission from about 2005 to 2012 and increased emission to 2017) is more than twice as large as shown in the CERES record. The larger variability in the FH record in the 1980 and 1990s, exclusive of that associated with Pinatubo in 1991–1993, may be related to more variability in the ISCCP satellite coverage; however Y.-C. Zhang et al. (2004) show that the monthly average SWup and LWup flux anomalies in the tropics for FD for 1985–1999 agree with those from the the Earth Radiation Budget Satellite record (Wielicki et al., 2002; Wong et al., 2006) to within about 1 Wm^{-2} (correlation about 0.8). Hence, some of the larger LW flux variation may be produced by the atmospheric temperature-humidity data set, rather than the cloud variations.

At the surface the global mean downwelling flux anomalies from FH are shown in Figure 3 (upper panel). As discussed in Rossow and Zhang (1995) and Y.-C. Zhang et al. (2010), such comparisons (with surface station observations) are affected by the point-to-area mismatch of atmospheric conditions, so we focus on only the larger scale tendencies. Several analyses of surface measurements of SWdn—spatial coverage limited to land stations—have suggested an overall decrease from about 1960 to about 1990 and an increase afterward into the early 2000s (Wild et al., 2005, cf. Wild, 2009). An increase after 2000 (to around 2008 and then a second increase after a short decrease) is consistent with the recent changes from CERES (Figure 2). The FH record for SWdn is qualitatively similar if trend lines are fit to the periods before Pinatubo and after 2000, but shows that the peak in the late 1990s is larger than the values after 2005. Pinker et al. (2005) show other similar results based on the ISCCP-D data with an increase from 1983 to about 2001.

The LWdn in FH shows a very large anomaly declining rapidly at the beginning of the record until the late 1990s. After that there is an increase by a little less than 2 Wm^{-2}. Stephens et al. (2012) calculate an increasing LWdn under clear conditions over ocean by 3 Wm^{-2} from 1988 to 2008, based on SST, column water vapor and CO_2 abundance determinations. The FH calculations (and previous versions) account for increasing CO_2 and CH_4 abundances, which should produce an increase in LWdn, all other things being equal; but as Figure 3 (lower panel) shows, the near-surface air temperature (Ta) and skin temperatures (Ts) from ISCCP-H used in FH are generally decreasing slightly. The magnitude of the decrease over the record is only about 1 K (well within the measurement uncertainty), but surface-based temperature records suggest an increase a little less than 1 K over this same period (GISTEMP Team, 2021). The air temperatures (and humidities not shown) in ISCCP-H and FH show a small downward trend and small ($\lesssim$1 K) discontinuities that are related to changes in the NNHIRS temperature and humidity retrievals between satellites in the High Resolution Infrared Radiation Sounder (HIRS) series; this behavior of the HIRS retrievals propagates into the FH LW results. The overall downward trend in FH LWdn at SRF is likely due to the properties of the atmospheric data used in the calculations, but the magnitude of the uncertainties, at least from the 1990s onward, is similar to the estimate shown in Table 1.

Overall, while these long-term results from FH might be taken to show good accuracy relative to direct measurements, especially for the SW fluxes, we emphasize that the disagreements shown in Figures 2 and 3 are well within the estimated uncertainties of both data sets.

Ever since the late 1980s, the ISCCP cloud data set has shown an overall decline of global mean CA, now also seen in other data sets (Karlsson & Devasthale, 2018). The decrease in ISCCP CA is about 0.06 from 1986 to 2018, which may be exaggerated by 0.01–0.02 by artifacts in earlier years (Rossow et al., 2022). The large variations in

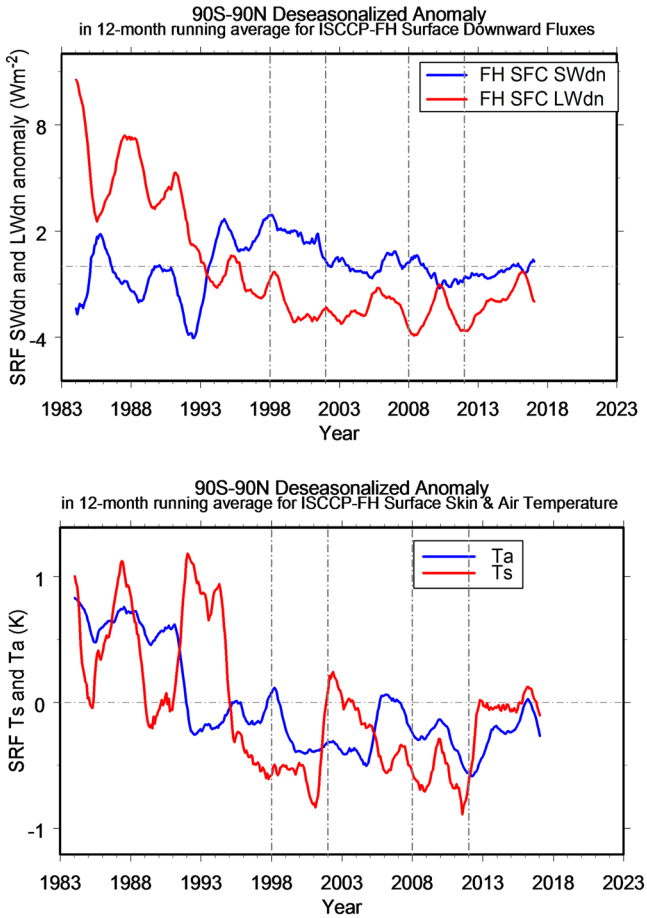

Figure 3. (Upper panel) Deseasonalized anomalies (shown as 12-month running averages) of global monthly mean downwelling Surface fluxes (Wm^{-2}) from FH for SWdn (blue curve) and LWdn (red curve). The anomalies for each data set are determined relative to their own record averages. (Lower panel) Deseasonalized anomalies (shown as 12-month running averages) of global monthly mean near-surface air temperature (TA, blue curve) and surface skin temperature (TS, red curve) in Kelvins from ISCCP-FH. The vertical lines delineate two time periods (1998–2002, 2008–2012) discussed later.

the early 1990s are caused by identification as cloud of some of the thick stratospheric aerosol from the Mt. Pinatubo volcano. Looking at the variations of cloud types, defined in ISCCP by combinations of cloud top pressure-optical thickness and phase, shows that the global decrease appears solely in the optically thinnest types, mostly cumulus (Cu) and altocumulus (Ac) with some cirrus (Ci), as shown in Figure 4 (as other cloud types show no changes, they are not shown). The results shown here are the version used in FH, where there have been adjustments of the ISCCP-H cloud type amounts that add some Cu amount and shift some middle-level clouds to cirrus to account for layer-overlap effects (cf. Rossow & Zhang, 2010), increasing/decreasing the magnitude of the Ci/Ac changes. As there is no corresponding increase in the optically thicker cloud types, this change is not consistent with a drift of the visible wavelength (VIS) calibration (cf. Rossow & Ferrier, 2015), even though the overall average optical thickness does increase because of the decreased amount of thinner clouds included in the average. Moreover, if a drift of VIS calibration were the cause, the changes in these three cloud types would be strongly correlated, but only the changes in Cu and Ac are correlated (coefficient $r \approx 0.8$), not Ci ($r < 0.4$ with Ac but $r \approx 0$ with Cu). The key is that total CA in the ISCCP data is insensitive to calibration changes (see Figure 2.2 in Appendix 2 in C. Stubenrauch et al., 2012) because the cloud detection each month is made relative to that month's determination of clear radiances: the global mean surface reflectance shows no trend. There is also supporting evidence from CERES, as shown in Figure 2, indicating a decline in the global mean albedo since the early 2000s (Loeb et al., 2021), and from an observed corresponding increase in surface solar insolation in the 1990s (Pinker et al., 2005; Wild et al., 2005).

Although the simultaneous variations of many cloud, atmosphere and surface properties effect the flux anomalies (Figures 2 and 3), the leading single-variable anomaly correlations (calculated for month-to-month variations over global maps at 110 km scale) are as follows (all other correlation values are much smaller). At TOA, the leading correlation with variations of SWnet is changes of Cu amount ($r \approx -0.5$), which are, in turn, correlated with T_S variations ($r \approx 0.7$, but this connection might be distorted by the fact that the T_S values come from satellite infrared measurements, which are clear-sky biased). The variations of SWcre are dominated by overall changes in optical thickness ($r \approx -0.8$). The TOA LWnet variations are strongly correlated with changes in Ac amount ($r \approx 0.7$) and secondarily with changes in mid-troposphere water vapor ($r \approx 0.5$); however, the changes in TOA LWcre are dominated by changes in Ci amount ($r \approx 0.8$) and near-surface air temperature, T_a ($r \approx 0.7$), but not the mid-troposphere temperature (T500 $r < 0.2$). Correlations of SRF SWnet are similar to those at TOA, but the SRF LWnet and LWcre are more correlated with temperature and humidity changes than with cloud changes (although Ci amount variations explain some of the LWcre variance). The ATM SWnet is much more strongly affected by atmospheric humidity changes (precipitable water at mid-troposphere, PW500 $r \approx 0.8$), but the SWcre changes are dominated by changes in Ci amount ($r \approx -0.8$). Likewise the ATM LWnet and LWcre are affected most by changes in atmospheric temperature ($r \approx -0.5$, 0.7 respectively, with T_a), although Ci amount is equally important to LWcre variations ($r \approx 0.8$).

6. Discussion of Some Possible Feedbacks Implied in an Example of Transient Change

The period from the late 1990s to the early 2010s is notable for a number of reasons: (a) it was framed at the beginning by a very strong El Nino in 1997–1998 and La Nina from 1999 to 2001 and at the end by a strong La Nina in 2010–2012 with some weaker events in between (www.cpc.ncep.noaa.gov/data/indices/oni.ascii.txt), (b) the Pacific Decadal Oscillation (PDO) index tracked the El Nino-Southern Ocillation (ENSO) index in these framing events from strongly positive switching to negative at the beginning to persistently negative at the end,

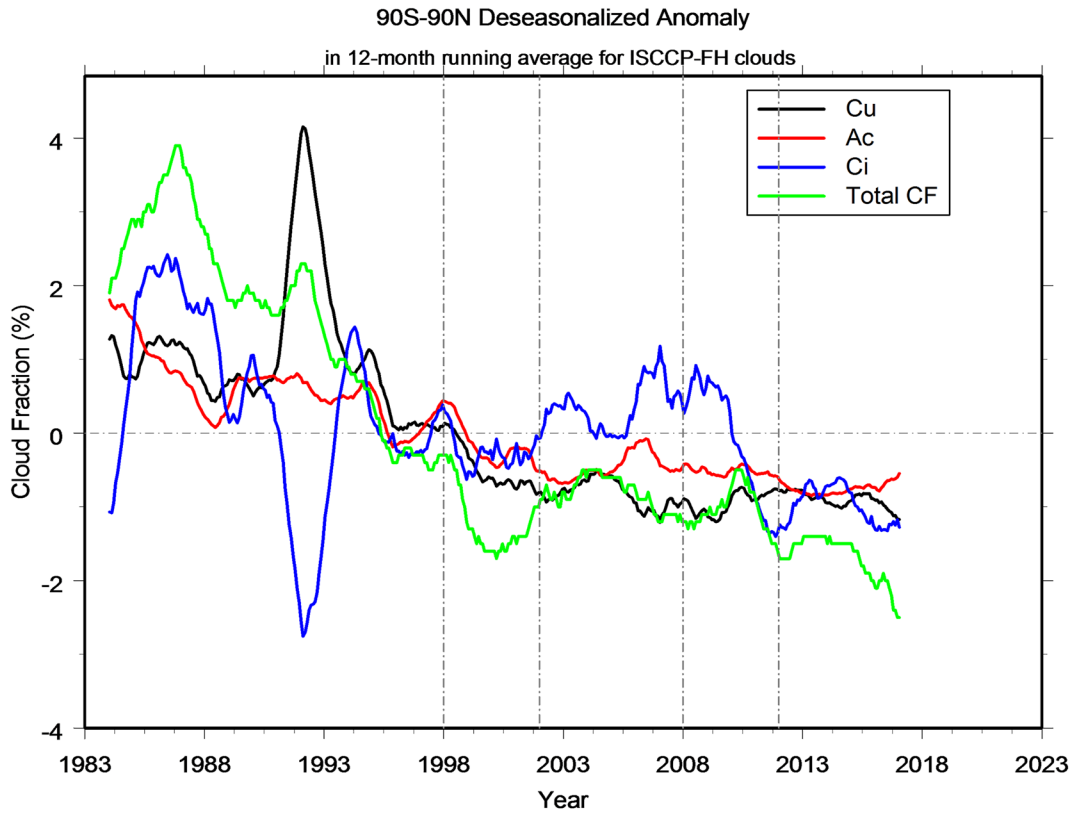

Figure 4. Deseasonalized anomalies (shown as 12-month running averages) of global monthly mean total (green curve) cloud amount (%) and the amounts of cirrus (blue curve), altocumulus (red curve) and cumulus (black curve) as defined by in ISCCP-H but modified for FH: added cumulus to account for upper-level-cloud overlap and shifted altocumulus to cirrus to account for effect of cloud overlap with cirrus.

but weakly positive in between (www.ncei.noaa.gov/pub/data/cmb/ersst/v5/index/ersst.v5.pdo.dat), and (c) there was a significant slowing of the rate of increase of global annual mean surface temperature as compared to the decades before and after this period (www.data.giss.nasa.gov/gistemp, see also Loeb et al., 2021). Figure 2 shows that the period from 1998 to 2012 was characterized in the FH data by a steady decrease of TOA SWnet (less heating) by a little more than 1.5 Wm^{-2} and an increase of TOA LWnet (less cooling) by a little more than 0.5 Wm^{-2}, giving an overall decrease TOA net flux by a little less than 1 Wm^{-2} (all quoted values are based on averages over 1998–2002 and 2008–2012 to represent the trends, Table 4). Figure 3 shows a very similar anomaly of SRF SWnet with no significant change of SRF LWnet in the period. Figure 4 shows a general increase of cirrus CA by almost 0.02 over this period (with a much smaller decrease of cumulus) and altocumulus, resulting in a near-constant total CA during this period.

Table 4
Mean Net Fluxes and Cloud Radiative Effects at TOA, at Surface and in Atmosphere for 1998–2002 and 2008–2012 Periods in Wm^{-2}

	SWnet	LWnet	Net	SWcre	LWcre	NETcre
TOA						
1998–2002 mean	237.1	−232.8	4.3	−48.0	26.3	−21.7
2008–2012 mean	235.5	−232.0	3.5	−49.8	26.8	−22.9
Surface						
1998–2002 mean	160.3	−53.4	107.0	−50.6	21.6	−29.0
2008–2012 mean	158.8	−53.5	105.3	−52.4	21.6	−30.8
Atmosphere						
1998–2002 mean	76.8	−179.4	−102.6	2.6	4.7	7.3
2008–2012 mean	76.8	−178.5	−101.8	2.7	5.2	7.9

Figure 5a shows the zonal mean distribution of total net radiation and cloud radiative effect (CRE) at TOA averaged over the two time periods (1998–2002, 2008–2012) that correspond (Figure 2), respectively, to the positive and negative anomalies of TOA SWnet and the negative and positive anomalies of TOA LWnet. The familiar total net flux distribution at TOA shows a net heating (|SWnet| > |LWnet|) in low to middle latitudes and a net cooling (|SWnet| < |LWnet|) at higher latitudes (cf. Y.-C. Zhang & Rossow, 1997; see also Kato et al., 2008). The net effect of clouds is to decrease lower latitude heating and increase higher latitude cooling (both negative CRE), except right at the poles where CRE is positive (cf. Y.-C. Zhang et al., 2004). The small SW and LW changes between these two periods (see Table 4) are accounted for by cloud changes; although other atmospheric and surface properties play

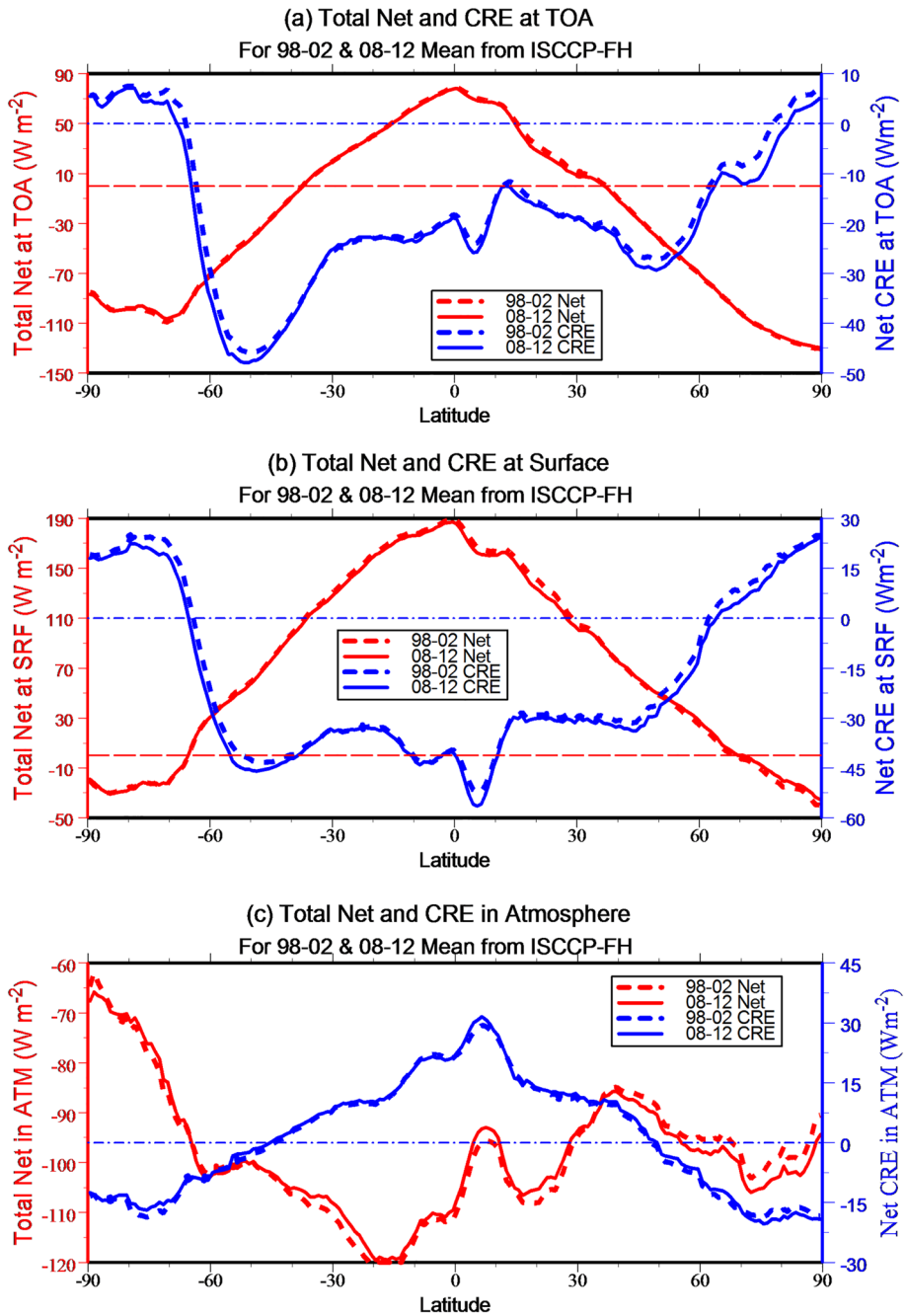

Figure 5. Zonal mean total net flux (red curves) and Cloud Radiative Effect (CRE, blue curves) in Wm^{-2} versus latitude averaged over two 5-yr periods (dashed curves 1998–2002, solid curves 2008–2012): (a) at TOA, (b) at surface and (c) in atmosphere. These two periods correspond, respectively, with positive and negative anomalies in TOA SWnet and negative and positive anomalies in TOA LWnet (Figure 2). See Table 4.

a role in the LW changes as discussed above (cf. Loeb et al., 2021), they are specifically related to the increase of cirrus in this particular period.

The global near-balance of TOA radiation splits into predominately SW heating of the surface and LW cooling of the atmosphere with clouds effects decreasing both as shown in Figures 5b and 5c and Tables 3 and 4 (cf. Y.-C. Zhang et al., 2004). The surface radiative heating (Figure 5b) decreases with latitude becoming net cooling in the annual mean only in the polar regions because of lack of solar heating in winter. The LW cooling at the polar surface is about 20–30 Wm^{-2} stronger in FH, the only significant change from FD. The new results are

much closer to surface measurements in the north (Persson et al., 2002), but are too strong by 10–20 Wm^{-2} in winter in the south (Van Den Broeke et al., 2005). The cloud effects at SRF decrease this heating at most latitudes (negative CRE) but cause surface heating at the poles (positive CRE). In other words clouds act to reduce the meridional gradient of surface heating that forces (in part) the oceanic circulation (cf. Kato et al., 2008; Matus & L'Ecuyer, 2017; Y.-C. Zhang & Rossow, 1997). The net atmospheric cooling (Figure 5c) is much larger at low to middle latitudes than in the polar regions (the polar cooling is much stronger in the north than in the south), overall following atmospheric temperature (more cooling at higher temperature). Clouds reduce the ATM cooling at low to middle latitudes (positive CRE) and enhance it in the polar regions (negative CRE). In other words clouds act to reduce the meridional gradient of atmospheric cooling, effectively enhancing the heating gradient that forces the atmospheric circulation (cf. Kato et al., 2008; Matus and L'Ecuyer. 2017; Y.-C. Zhang & Rossow, 1997).

All of the decrease of TOA SWnet (less heating) between 1998 and 2012 occurred at SRF and all of the increase of TOA LWnet (less cooling) occurred in the atmosphere (Table 4). The corresponding very small changes in the latitudinal distribution of net fluxes and CRE in Figure 5 are better shown in Figure 6 as the differences, 2008–2012 average minus 1998–2002 average, representing the trend from 1998 to 2012. The global average decrease of TOA total net flux over this period appears as a decrease at low to middle latitudes, but there is also an increase (reduced cooling) in the polar regions (Figure 6a). The global mean decrease of total net flux at TOA is caused almost entirely by cloud effects on the SW offset by a weak effects on LW: Figure 6a shows that the CRE difference is (mostly) negative at all latitudes but much more so at higher latitudes. However the changes in TOA total net flux conflate changes in SW forcing at the surface with changes in the LW response of the atmosphere, so separating the TOA changes into their SRF and ATM components better reveals what happened between 1998 and 2012. To keep the signs straight in what follows, the surface net flux changes are described as increases/decreases of heating and the atmospheric net flux changes are described as increases/decreases of cooling.

The net flux changes at SRF from 1998 to 2002 to 2012–2016 (Figure 6b) show a very different pattern in the two hemispheres. The heating in the tropics decreased (negative difference), more strongly in the north than the south; the cooling at the poles also decreased (positive difference), again more strongly in the north than the south. These differences represent a decrease in the equator-to-pole heating gradient over this period. At middle latitudes the surface heating decreased in the southern hemisphere and increased in the northern hemisphere, but this pattern seems consistent with the overall change of the PDO index from positive to negative over this period, which would be a negative change of sea surface temperature (SST) in the tropical Pacific and positive change of SST in the north Pacific. The overall pattern of change implies a weaker meridional gradient in radiative heating forcing of the oceanic circulation, consistent with the cooling (warming) of SST in the tropics (midlatitudes). These net flux changes are opposed by the cloud changes: negative SRF CRE at lower latitudes shows only a very small decrease (becoming more negative) in the tropics and subtropics, but more substantial decreases at higher midlatitudes, related to the small decrease of cumulus and altocumulus clouds. Near the poles, where the SRF Net switches from negative to positive, it also decreases (becoming less positive). The CRE on surface heating is caused by decreased cumulus and altocumulus amounts. If the cloud-induced radiative flux changes from 1998 to 2012—a smaller cloud-induced decrease of the meridional heating gradient (i.e., tending to make the heating gradient larger)—are indirectly related (through ocean-atmosphere interaction) to a change of the ocean circulation associated with the reduced meridional temperature gradient (positive to negative PDO index), then they imply a positive cloud-radiative feedback on the ocean circulation.

From 1998–2002 to 2008–2012, the ATM cooling decreased at lower latitudes (positive difference, a heating) and increased at higher latitudes (negative difference, a cooling), especially in the northern hemisphere (Figure 6c). This implies an enhancement of the meridional radiative cooling gradient forcing the atmospheric circulation. The positive ATM CRE at low latitudes slightly increased (more heating related to increased cirrus) and the negative ATM CRE in the polar regions behaved differently in the north and south, decreasing in the north (decreased cooling effect) and increasing in the south (increased cooling effect). If these cloud-radiative changes are caused by a weakening of the atmospheric circulation, as might be expected from the decrease of the SST meridional gradient with the PDO phase change (see J. Chen et al., 2002 that find a strengthening circulation for an opposite trend in the 1990s), then the cloud changes imply a negative feedback on the atmospheric circulation.

The opposite sense of these (possible) transient cloud-radiative feedbacks on the coupled atmospheric and oceanic circulations on a decadal time scale comes about because of the separate SW heating of SRF and LW cooling of ATM and because of the different SW and LW CRE by different cloud types. A similar opposite effect

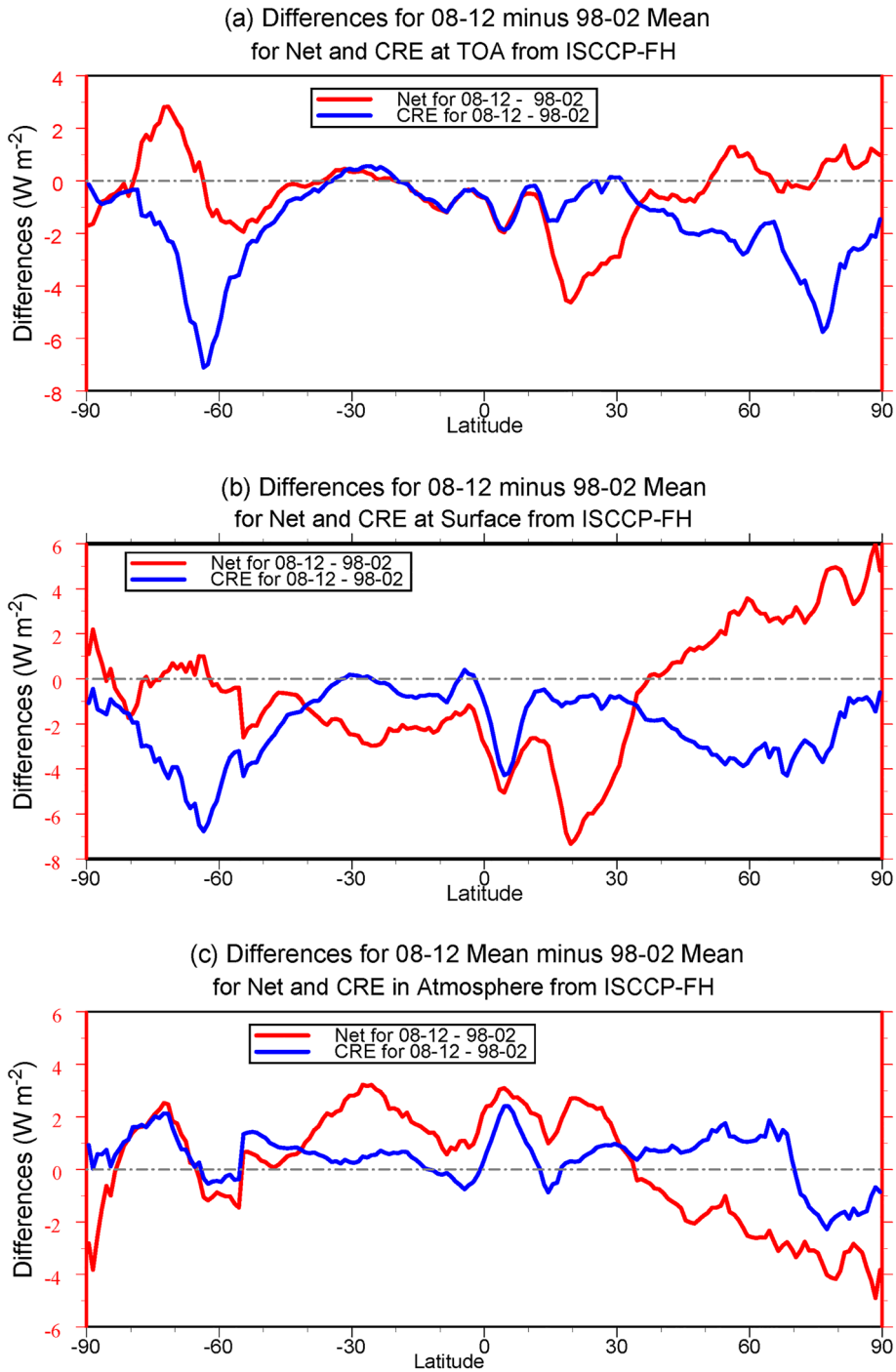

Figure 6. Differences between two 5-yr periods (2008–2012 minus 1998–2002) of the zonal mean total net flux (red curve) and atmosphere CRE (blue curve) in Wm^{-2} versus latitude: (a) at TOA, (b) at surface and (c) in atmosphere.

is seen in the partitioning of average cloud-radiative effects on the mean circulations discussed in Y.-C. Zhang and Rossow (1997) and Kato et al. (2008).

7. Conclusions

There are now three global data products that provide calculated, cloud-modified, atmospheric radiative heating rate profiles: one based on CloudSat/CALIPSO (2B-FLXHR, L'Ecuyer et al., 2008, also L'Ecuyer et al., 2019

and Hang et al., 2019), one based on CERES (latest version, Ed4.0, described in Loeb et al. (2018)) and one based on ISCCP-H, called FH reported here (see also Y.-C. Zhang, 2017), a revised version of ISCCP-FD (Y.-C. Zhang et al., 2004). The calculated flux profiles in the first product are based on direct radar-lidar measurements from satellites of cloud layer location and thickness, as well as estimates of cloud water content, with very high vertical resolution, covering 4 years at twice-daily sampling, but with very sparse spatial sampling (e.g., L'Ecuyer et al., 2008, show that their calculated TOA fluxes exhibit the best agreement with CERES results when averaged to spatial intervals of 5° and over a whole year). The combined radar-lidar measurements still slightly underestimate the amount of very low-level cloudiness because of ground-clutter effects on the radar measurements (L'Ecuyer et al., 2008) and because some low cloudiness is hidden below thicker upper-level clouds that the lidar cannot penetrate (Henderson et al., 2013, evaluate the effects of the estimated missed cloud amounts). The calculated flux profiles in the CERES products cover a longer time period (currently about 20 yr) and are constrained by direct, four-times-daily TOA flux measurements. These flux profiles employ additional satellite cloud products and reanalysis model atmospheric properties to interpolate the direct measurements to 1-hr time intervals, effectively assuming single-layer clouds in each scene with no detail below the 500 hPa level (Rose et al., 2013). While the TOA SW flux is a strong constraint on the calculated CERES profiles of SW, the TOA LW flux is a much weaker constraint. Haynes et al. (2013) contrast the high vertical resolution of the 2B-FLXHR heating rate profile with the very low vertical resolution CERES product in their Figure 1.

The horizontal lines in Figure 1 indicate the vertical intervals in the FH (and FD) profiles, both of which augment the ISCCP cloud type information with a statistical CVL model accounting for cloud layer overlap (revised for FH based on RL-GEOPROF). Although still crude in the vertical compared to 2B-FLXHR profiles but with much better space-time sampling, the FH (and FD) profiles still capture the basic low-middle-high features of the cloud distribution in the figure. Based on the sensitivity studies of the effects of changing cloud vertical layers on the flux profiles, discussed in Section 4, the long-term changes in three cloud types shown in Figure 4 imply the following: the decrease of cumulus and altocumulus decreases LWnet in the lower atmosphere and surface by <3 Wm^{-2} reinforced by a smaller decrease of cirrus that also causes a similar magnitude net flux decrease in the upper atmosphere. The SW flux profile is insensitive to such small changes. Overall, the long-term change in clouds do not appear to have changed the radiative flux profile shapes in the global mean, but regional changes may be more significant. However, decrease of low CA shows up as a decrease of SRF LWdn in Figure 3a. Looking at the longer FH record, the overall decrease in cumulus and altocumulus amounts appears to be offset by a small increase in cloud optical thickness (see Figure 5 in Rossow et al., 2022) such that SWnet heating at TOA and SRF increased slightly and the LWnet cooling at TOA/ATM (SRF) increased (decreased) (Figures 2 and 3). However, these changes, if accurate, are all <2 Wm^{-2}.

As discussed here, the overall estimated uncertainty of monthly average regional (110 km scale) FH fluxes increases from <10 W/m^2 at TOA up to <15 W/m^2 at the surface; the uncertainties at intermediate levels are in between these two. Although differences between FH fluxes and the matched direct measurements at 110 km and 3 hr scales are larger, the scatter with the comparison measurements appears to be caused more by mismatched spatial scales, meteorological conditions, and observation times (cf. Rossow & Zhang, 1995; Y.-C. Zhang et al., 2004; Y.-C. Zhang et al., 2010 for more detailed evaluations). Typical magnitudes of flux variation at this smaller scale are generally larger (10's of Wm^{-2}) than the estimated uncertainties, produced mostly by cloud variations, which are larger in time than space because the CA distribution is "U-shaped" (cf. Rossow & Cairns, 1995; Rossow et al., 1993) with CA <0.1 occurring more than 15% and >0.9 more than 40% of the time. There are some surface regimes (LW in polar and tropical areas) where the FH space-time flux variations are smaller than the estimated uncertainties, which suggests that our estimates of random uncertainty are conservative. The main limitation of FH accuracy in the SW is related to variations of the cloud microphysical properties (which are fixed in the calculations), especially for ice clouds. In LW, especially at the surface, the main limitation is related to the uncertainty in the ancillary atmospheric temperature-humidity data.

The accuracy of the FH fluxes is still sufficient, compared with the magnitude of local (110 km), 3-hourly variations, for diagnosing weather-to-seasonal scale variations of radiation induced by changes in cloudiness as well as atmospheric and surface properties. Together with the variety of other satellite measurements, especially multi-spectral imagers, infrared spectrometers, microwave temperature-humidity sounders and active cloud and precipitation profilers, these results can be combined with global reanalyzes of atmospheric motions to diagnose energy and water exchanges in the whole range of weather systems, for example, analyses such as Jacob & Schumacher (2008), Haynes et al. (2011), Oreopoulos & Rossow (2011), Booth et al. (2013), Polly and

Rossow (2016), Masunaga and Luo (2016), and Rossow et al. (2016), and those associated with slower "climate" variations such as Madden-Julian Oscillation, seasons, and ENSO events, for example, analyses such as Y.-C. Zhang and Rossow (1997), Kato et al. (2008), and Tromeur and Rossow (2010). The clouds and radiative flux effects in weather and climate models can be evaluated, for example, Tselioudis et al., 2021.

On the larger scale of interannual variations of the atmospheric and oceanic general circulations, these newer radiative flux products can be combined with newer global data sets quantifying precipitation, water vapor, surface turbulent fluxes, ocean surface and atmospheric winds, and temperatures to calculate the mean energy and water transports (updating Kato et al., 2008; Y.-C. Zhang & Rossow, 1997 e.g., see also Stephens et al., 2016). The general energetics of the atmospheric circulation can also be determined (updating Romanski & Rossow, 2013 e.g.,). An example of such a data collection is the 15-yr GEWEX Integrated Data Product (Kummerow et al., 2019). Direct quantitative diagnosis of the transient feedbacks on these circulations and exchanges by cloud processes is now possible. The advantage of using ISCCP-FH for such studies, in addition to the higher time resolution and longer record than other products, is that the causes of variations in radiative heating of the atmosphere and surface can be made directly, separating cloud effects from other causes at weather-to-interannual scales.

Data Availability Statement

ISCCP-FH flux profile data products and documents can be accessed and downloaded through login at https://isccp.giss.nasa.gov/projects/flux.html. CERES SYN1deg Ed4 data may be ordered from https://ceres.larc.nasa.gov/data/#syn1deg-level-3, and for data Quality Summary, see https://ceres.larc.nasa.gov/documents/DQ_summaries/CERES_SYN1deg_Ed4A_DQS.pdf. (Registration is required). BSRN data can be obtained from https://bsrn.awi.de/other/publications/establishment-and-development-of-the-bsrn/. (Registration is required).

Acknowledgments
We would like to give special thanks to Dr. Reto Reudy who helped separate the radiation code (RadE) from NASA GISS GCM ModelE that makes possible to initiate the ISCCP-FH project. We also especially thank Dr. Andrew A. Lacis and Dr. Valdar Oinas who participated in the development of the radiation code for the ISCCP-FH project that made possible the ISCCP-FH flux data production. The development of the ISCCP-FH production code was funded by NOAA Climate Data Record Project (Grant NA11NES4400002 for 2011–2014). Computer facilities are supplied by NOAA's National Centers for Environmental Information and NASA Goddard Institute for space Studies. We thank Dr. Stefan Kinne who has provided us with Aerocom, MACv1 and MACv2, aerosol data sets. We also thank Dr. Paul W. Stackhouse and Dr. Shashi K. Gupta who have provided us with TSI data sets. Finally we thank CERES and BSRN teams for providing us with their data sets for the evaluation of the ISCCP-FH products. We thank the three anonymous reviewers for their many beneficial and important comments, critiques, suggestions and questions that help improve the paper.

References

Barkstrom, B., Harrison, E., Smith, G., Green, R., Kibler, J., Cess, R., & the ERBE Science Team. (1989). Earth radiation budget experiment (ERBE) archival and April 1985 results. *Bulletin America Meteorology Social*, *70*(10), 1254–1262. https://doi.org/10.1175/1520-0477(1989)070<1254:erbeaa>2.0.co;2

Booth, J. F., Naud, C. M., & Del Genio, A. D. (2013). Diagnosing warm frontal cloud formation in a GCM: A novel approach using conditional subsetting. *Journal of Climate*, *26*(16), 5827–5845. https://doi.org/10.1175/jcli-d-12-00637.1

CERES Science Team. (2013). CERES_SYN1deg_Ed3A data quality summary. Retrieved from https://ceres.larc.nasa.gov/documents/DQ_summaries/CERES_SYN1deg_Ed3A_DQS.pdf

Chen, J., Carlson, B. E., & Del Genio, A. D. (2002). Evidence for the strengthening of the tropical general circulation in 1990s. *Science*, *295*(5556), 838–841. https://doi.org/10.1126/science.1065835

Chen, T., & Rossow, W. B. (2002). Determination of top-of-atmosphere longwave radiative fluxes: A comparison between two approaches using ScaRab data. *Journal of Geophysical Research*, *107*(D8), 1–14. https://doi.org/10.1029/2001jd000914

Chen, T., Zhang, Y.-C., & Rossow, W. B. (2000). Sensitivity of atmospheric radiative heating rate profiles to variations of cloud layer overlap. *Journal of Climate*, *13*(16), 2941–2959. https://doi.org/10.1175/1520-0442(2000)013<0264:reoctv>2.0.co;2

DeAngelis, A. M., Qu, X., Zelinka, M. D., & Hall, A. (2015). An observational radiative constraint on hydrologic cycle intensification. *Nature*, *528*(7581), 249–253. https://doi.org/10.1038/nature15770

Driemel, A., Augustine, J., Behrens, K., Colle, S., Cox, C., Cuevas-Agulló, E., et al. (2018). Baseline surface radiation network (BSRN): Structure and data description (1992–2017). *Earth System Science Data*, *10*(3), 1491–1501. https://doi.org/10.5194/essd-10-1491-2018

GISTEMP Team. (2021). *GISS surface temperature analysis (GISTEMP), version 4*. Dataset. NASA Goddard Institute for Space Studies. Retrieved from https://data.giss.nasa.gov/gistemp/

Goode, P. R., Palle, E., Shoumko, A., Shoumko, S., Montanes-Rodriguez, P., & Koonin, S. E. (2021). Earth's albedo 1998-2017 as measured from earthshine. *Geophysical Research Letters*, *48*(1–8), e2021GL094888. https://doi.org/10.1029/2021gl094888

Hang, Y., L'Ecuyer, T. S., Henderson, D., Matus, A. V., & Wang, Z. (2019). Reassessing the role of cloud type in Earth's radiation budget after a decade of active spaceborne observations. Part II: Atmospheric heating. *Journal of Climate*, *32*(19), 6219–6236. https://doi.org/10.1175/jcli-d-18-0754.1

Hansen, J., Fung, I., Lacis, A., Rind, D., Lebedeff, S., Ruedy, R., et al. (1988). Global climate changes as forecast by the Goddard Institute for Space Studies three-dimension model. *Journal of Geophysical Research*, *93*(D8), 9341–9364. https://doi.org/10.1029/jd093id08p09341

Haynes, J. M., Jakob, C., Rossow, W. B., Tselioudis, G., & Brown, J. (2011). Major characteristics of southern ocean cloud regimes and their effects on the energy budget. *Journal of Climate*, *24*(19), 5061–5080. https://doi.org/10.1175/2011jcli4052.1

Haynes, J. M., Vonder Haar, T. H., L'Ecuyer, T., & Henderson, D. (2013). Radiative heating characteristics of Earth's cloudy atmosphere from vertically resolved active sensors. *Geophysical Research Letters*, *40*(3), 624–630. https://doi.org/10.1002/grl.50145

Henderson, D. S., L'Ecuyer, T., Stephens, G., Partain, P., & Sekiguchi, M. (2013). A multisensor perspective on the radiative impacts of clouds and aerosols. *Journal of Applied Meteorology and Climatology*, *52*(4), 853–871. https://doi.org/10.1175/jamc-d-025.1

Jacob, C., & Schumacher, C. (2008). Precipitation and latent heating characteristics of the major tropical western Pacific cloud regimes. *Journal of Climate*, *21*(17), 4348–4364. https://doi.org/10.1175/2008jcli2122.1

Jin, Y., & Rossow, W. B. (1997). Detection of cirrus overlapping low-level clouds. *Journal of Geophysical Research*, *102*(D2), 1727–1737. https://doi.org/10.1029/96jd02996

Karlsson, K.-G., & Devasthale, A. (2018). Inter-comparison and evaluation of the four longest satellite-derived cloud climate data records: CLARA-A2, ESA Cloud CCI V3, ISCCP-HGM and PATMOS-x. *Remote Sensing*, *10*(1567), 1–27. https://doi.org/10.3390/rs10101567

Kato, S., Rose, F. G., Rutan, D. A., & Charlock, T. P. (2008). Cloud effects on the meridional atmospheric energy budget estimated from Clouds and the Earth's Radiant Energy (CERES) data. *Journal of Climate*, *21*(17), 4223–4241. https://doi.org/10.1175/2008jcli1982.1

Kelley, M., Schmidt, G. A., Nazarenko, L. S., Bauer, S. E., Ruedy, R., Russell, G. L., et al. (2020). GISS-E2.1: Configurations and climatology. *Journal of Advances in Modeling Earth Systems*, *12*(8), e2019MS002025. https://doi.org/10.1029/2019MS002025

Kinne, S. (2019). The MACv2 aerosol climatology. *Tellus B: Chemical and Physical Meteorology*, *71*(1), 1–21. https://doi.org/10.1080/16000889.2019.1623639

Kinne, S., O'Donnel, D., Stier, P., Kloster, S., Zhang, K., Schmidt, H., et al. (2013). MAC-v1: A new aerosol climatology for climate studies. *Journal of Advances in Modeling Earth Systems*, *5*(4), 704–740. https://doi.org/10.1002/jame.20035.2013

Kohsiek, W., Liebenthal, C., Foken, T., Vogt, R., Oncley, S. P., Bernhofer, C., & Debruin, H. A. R. (2006). The Energy Balance Experiment EBEX-2000. Part III: Behavior and quality of the radiation measurements. *Boundary-Layer Meteorology*, 1–21. https://doi.org/10.1007/s10546-006-9135-8

Kummerow, C., Brown, P., Adler, R., Kinne, S., Rossow, W., Stackhouse, P., et al. (2019). The GDAP integrated product. *GEWEX News*, *29*, 3–6.

Lacis, A. A., & Oinas, V. (1991). A description of the correlated k distributed method for modeling nongray gaseous absorption, thermal emission, and multiple scattering in vertically inhomogeneous atmospheres. *Journal of Geophysical Research*, *96*(D5), 9027–9063. https://doi.org/10.1029/90jd01945

L'Ecuyer, T. S., Hang, Y., Matus, A. V., & Wang, Z. (2019). Reassessing the role of cloud type in Earth's radiation budget after a decade of active spaceborne observations. Part I: Top of atmosphere and surface. *Journal of Climate*, *32*(19), 6197–6217. https://doi.org/10.1175/jcli-d-18-0753.1

L'Ecuyer, T. S., Wood, N., Haladay, T., & Stephens, G. L., & Stackhouse, P. W. (2008). The impact of clouds on atmospheric heating based on the R04 CloudSat fluxes and heating rate data set. *Journal of Geophysical Research*, *113*, D00A15. https://doi.org/10.1029/2008JD009951

Liao, X., Rossow, W. B., & Rind, D. (1995). Comparison between SAGE II and ISCCP high-level clouds, Part II: Locating cloud tops. *Journal of Geophysical Research*, *100*(D1), 1137–1147. https://doi.org/10.1029/94jd02430

Liu, Z., Kar, J., Zeng, S., Tackett, J., Vaughan, M., Avery, M., et al. (2019). Discriminating between clouds and aerosols in the CALIOP version 4.1 data products. *Atmospheric Measurement Techniques*, *12*(1), 703–734. https://doi.org/10.5194/amt-12-703-2019

Loeb, N. G., Doelling, D. R., Wang, H., Su, W., Nguyen, C., Corbett, J. G., et al. (2018). Clouds and the Earth's Radiant Energy System (CERES) Energy Balanced and Filled (EBAF) top-of-atmosphere (TOA) Edition-4.0 data product. *Journal of Climate*, *31*(2), 894–918. https://doi.org/10.1175/jcli-d-17-0208.1

Loeb, N. G., Johnson, G. C., Thorsen, T. J., Lyman, J. M., Rose, F. G., & Kato, S. (2021). Satellite and ocean data reveal marked increase in Earth's heating rate. *Geophysical Research Letters*, *48*(13), 1–8. https://doi.org/10.1029/2021gl093047

Loeb, N. G., Priestley, K. J., Kratz, D. P., Geier, E. B., Green, R. N., Wielicki, B. A., et al. (2001). Determination of unfiltered radiances from the Clouds and the Earth's Radiant Energy System instrument. *Journal of Applied Meteorology*, *40*(4), 822–835. https://doi.org/10.1175/1520-0450(2001)040<0822:dourft>2.0.co;2

Loeb, N. G., Wielicki, B. A., Doelling, D. A., Smith, G. L., Keyes, D. F., Kato, S., et al. (2009). Toward optimal closure of Earth's top-of-atmosphere radiation budget. *Journal of Climate*, *22*(3), 748–766. https://doi.org/10.1175/2008jcli2637.1

Mace, G. G., & Zhang, Q. (2014). The CloudSat radar-lidar geometric profile product (RL-GeoProf): Updates, improvements, and selected results. *Journal of Geophysical Research: Atmospheres*, *119*(15), 9441–9462. https://doi.org/10.1002/2013jd021374

Masunaga, H., & Luo, Z. J. (2016). Convective and large-scale mass flux profiles over tropical oceans determined from synergistic analysis of a suite of satellite observations. *Journal of Geophysical Research: Atmospheres*, *121*(13), 7958–7974. https://doi.org/10.1002/2016jd024753

Matus, A. V., & L'Ecuyer, T. (2017). The role of cloud phase in Earth's radiation budget. *Journal of Geophysical Research: Atmospheres*, *122*(5), 2559–2578. https://doi.org/10.1002/2016jd025951

Michalsky, H., Dutton, E., Rubes, M., Nelson, D., Stoffel, T., Wesley, M., et al., (1999). Optimal measurement of surface shortwave irradiance using current instrumentation. *Journal of Atmospheric and Oceanic Technology*, *16*(1), 55–69. https://doi.org/10.1175/1520-0426(1999)016<0055:omossi>2.0.c0;2

Ohmura, A., Dutton, E. G., Forgan, B., Frohlich, C., Gilgen, H., Hegner, H., et al. (1998). Baseline Surface Radiation Network (BSRN/WCRP): New precision radiometry for climate research. *Bulletin America Meteorology Social*, *79*(10), 2115–2136. https://doi.org/10.1175/1520-0477(1998)079<2115:bsrnbw>2.0.co;2

Oreopoulos, L., Mlawer, E., Delamere, J., Shippert, T., Cole, J., Fomin, B., et al. (2012). The continual intercomparison of radiation codes: Results from phase I. *Journal of Geophysical Research*, *117*(D6), D06118. https://doi.org/10.1029/2011jd016821

Oreopoulos, L., & Rossow, W. B. (2011). The cloud radiative effect of ISCCP weather states. *Journal of Geophysical Research*, *116*(1–22), D12202. https://doi.org/10.1029/2010jd015472

Persson, P. O. G., Fairall, C. W., Andreas, E. L., Guest, P. S., & Perovich, D. K. (2002). Measurements near the atmospheric surface flux group tower at SHEBA: Near-surface conditions and surface energy budget. *Journal of Geophysical Research*, *107*(8045), 1–21. https://doi.org/10.1029/2000jc000705

Philipona, R., Dutton, E. G., Stoffel, T., Michalsky, J., Reda, I., Stifter, A., et al. (2001). Atmospheric longwave radiance uncertainty: Pyrgeometers compared to an absolute sky-scanning radiometer, atmospheric emitted radiance interferometer, and radiative transfer model calculations. *Journal of Geophysical Research*, *106*(D22), 28129–28141. https://doi.org/10.1029/200jd000196

Pinker, R. T., Zhang, B., & Dutton, E. G. (2005). Do satellites detect trends in surface solar radiation? *Science*, *308*(5723), 850–854. https://doi.org/10.1126/science.1103159

Polly, J., & Rossow, W. B. (2016). Distribution of midlatitude cyclone attributes based on the MCMS database. *Journal of Climate*, *29*(18), 6483–6507. https://doi.org/10.1175/jcli-d-15-0857.1

Protat, A., Young, S. A., McFarlane, S. A., L'Ecuyer, T., Mace, G. G., Comstock, J. M., et al. (2014). Reconciling ground-based and space-based estimates of the frequency of occurrence and radiative effect of clouds around Darwin, Australia. *Journal of Applied Meteorology and Climatology*, *53*(2), 456–478. https://doi.org/10.1175/jamc-d-13-072.1

Raschke, E., Kinne, S., Rossow, W. B., Stackhouse, P. W., & Wild, M. (2016). Comparison of radiative energy flows in observational datasets and climate modeling. *Journal of Applied Meteorology and Climatology*, *55*(1), 93–117. https://doi.org/10.1175/jamc-d-14-0281.1

Raschke, E., Kinne, S., & Stackhouse, P. W. (2012). GEWEX radiation flux assessment (RFA), WCRP report 19/2012, Vol. 1. *Scientific Results*, *2*. Appendices and details Retrieved from http://www.wcrp-climate.org/documents/GEWEX RFA-Volume 1-report.pdf

Romanski, J., & Rossow, W. B. (2013). Contributions of individual atmospheric diabatic heating processes to the generation of available potential energy. *Journal of Climate*, *26*(12), 4244–4263. https://doi.org/10.1175/jcli-d-12-00457.1

Rose, F. G., Rutan, D. A., Charlock, T., Smith, G. L., & Kato, S. (2013). An algorithm for the constraining of radiative transfer calculations to CERES-observed broadband to-of-atmosphere irradiance. *Journal of Atmospheric and Oceanic Technology*, *30*(6), 1091–1106. https://doi.org/10.1175/jtech-d-12-00058.1

Rossow, W. B. (2017). ISCCP H-version—Climate algorithm theoretical basis document, NOAA climate data record program (CDRP-ATDB-0.872) Rev 0 (p. 301). Retrieved from http://www1.ncdc.noaa.gov/pub/data/sds/cdr/CDRs/Cloud_Properties-ISCCP/AlgorithmDescription_01B-29.pdf

Rossow, W. B., & Cairns, B. (1995). Monitoring changes of clouds. *Climatic Change*, *31*, 305–347. https://doi.org/10.1007/978-94-011-0323-7_11

Rossow, W. B., & Ferrier, J. (2015). Evaluation of long-term calibrations of the AVHRR visible radiances. *Journal of Atmospheric and Oceanic Technology*, *32*(4), 744–766. https://doi.org/10.1175/jtech-d-14-00134.1

Rossow, W. B., Knapp, K. R., & Young, A. H. (2022). International satellite cloud climatology project: Extending the record. *Journal of Climate*, *35*, 141–158. https://doi.org/10.1175/jcli-d-21-0157.1

Rossow, W. B., Walker, A. W., & Garder, L. C. (1993). Comparison of ISCCP and other cloud amounts. *Journal of Climate*, *6*(12), 2394–2418. https://doi.org/10.1175/1520-0442(1993)006<2394:coiaoc>2.0.co;2

Rossow, W. B., & Zhang, Y.-C. (1995). Calculation of surface and top-of-atmosphere radiative fluxes from physical quantities based on ISCCP datasets, Part II: Validation and first results. *Journal of Geophysical Research*, *100*(D1), 1167–1197. https://doi.org/10.1029/94jd02746

Rossow, W. B., & Zhang, Y.-C. (2010). Evaluation of a statistical model of cloud vertical structure using combined CloudSat and CALIPSO cloud layer profiles. *Journal of Climate*, *23*(24), 6641–6653. https://doi.org/10.1175/2010jcli3734.1

Rossow, W. B., Zhang, Y.-C., & Tselioudis, G. (2016). Atmospheric diabatic heating in different weather states and the general circulation. *Journal of Climate*, *29*(3), 1059–1065. https://doi.org/10.1175/jcli-d-15-0760.1

Rossow, W. B., Zhang, Y.-C., & Wang, J.-H. (2005). A statistical model of cloud vertical structure based on reconciling cloud layer amounts inferred from satellites and radiosonde humidity profiles. *Journal of Climate*, *18*(17), 3587–3605. https://doi.org/10.1175/jcli3479.1

Rothman, L. S., & coauthors (2013). The HITRAN2012 molecular spectroscopic database. *Journal of Quantitative Spectroscopy and Radiative Transfer*, *130*, 4–50.

Stackhouse, P. W., Cox, S. J., Mikovitz, J. C., & Zhang, T. (2021). GEWEX (global energy and water exchanges project) surface radiation budget (SRB) release 4 integrated product (IP4) algorithm theoretical basis document and evaluation. Retrieved from https://asdc.larc.nasa.gov/documents/srb/SRB_Rel4-IP_ATBD.pdf

Stephens, G. L., Hakuba, M. Z., Hawcroft, M., Haywood, J. M., Behrangi, A., Kay, J. E., & Webster, P. J. (2016). The curious nature of the hemispheric symmetry of the Earths' energy and water balances. *Current Climate Change Reports*, *2*(4), 135–147. https://doi.org/10.1007/s40641-016-0043-9

Stephens, G. L., Hakuba, M. Z., Kato, S., Gettelman, A., Dufesne, J.-J., Andrews, T., et al. (2022). The changing nature of Earth's reflected sunlight. *Proceedings of the Royal Society A*, *478*(2263), 20220053. https://doi.org/10.1098/rspa.2022.0053

Stephens, G. L., Wild, M., Stackhouse, P. W., L'Ecuyer, T., Kato, S., & Henderson, D. S. (2012). The global character of the flux of downward longwave radiation. *Journal of Climate*, *25*(7), 2329–2340. https://doi.org/10.1175/jcli-d-11-00262.1

Stubenrauch, C., Rossow, W. B., & Kinne, S. (2012). GEWEX assessment of global cloud data sets from satellites. *WCRP*, 176.

Stubenrauch, C. J., Rossow, W. B., Kinne, S., Ackerman, S. A., Cesana, G., Chepfer, H., et al. (2013). Assessment of global cloud datasets from satellites: Project and database initiated by the GEWEX radiation panel. *Bulletin America Meteorology Social*, *94*(7), 1031–1049. https://doi.org/10.1175/bams-d-12-00117.1

Su, W., Corbett, J., Eitzen, Z., & Liang, L. (2015a). Next-generation angular distribution models for top-of-atmosphere radiative flux calculations from CERES instruments: Methodology. *Atmospheric Measurement Techniques*, *8*(2), 611–632. https://doi.org/10.5194/amt-8-611-2015

Su, W., Corbett, J., Eitzen, Z., & Liang, L. (2015b). Next-generation angular distribution models for top-of-atmosphere radiative flux calculations from CERES instruments: Validation. *Atmospheric Measurement Techniques*, *8*, 3297–3313. https://doi.org/10.5194/amt-8-3297-2015

Tromeur, E., & Rossow, W. B. (2010). Interaction of tropical deep convection with the large-scale circulation in the Madden-Julian oscillation. *Journal of Climate*, *23*(7), 1837–1853. https://doi.org/10.1175/202009jcli3240.1

Tselioudis, G., Rossow, W. B., Jakob, C., Remillard, J., Tropf, D., & Zhang, Y.-C. (2021). Evaluation of clouds, radiation, and precipitation in CMIP6 models using global weather states derived from ISCCP-H cloud property data. *Journal of Climate*, *34*, 7311–7324. https://doi.org/10.1175/jcli-d-21-0076.1

Van Den Broeke, M., Reijmer, C., Van As, D., Van De Wal, R., & Oerlemans, J. (2005). Seasonal cycles of Antarctic surface energy balance from automatic weather stations. *Annals of Glaciology*, *41*, 131–139. https://doi.org/10.3189/172756405781813168

Wang, J., Rossow, W. B., & Zhang, Y.-C. (2000). Cloud vertical structure and its variations from a 20-year global rawinsonde dataset. *Journal of Climate*, *13*(17), 3041–3056. https://doi.org/10.1175/1520-0442(2000)013<3041:cvsaiv>2.0.co;2

Wielicki, B. A., Wong, T., Allan, R. P., Slingo, A., Kiehl, J. T., Soden, B. J., et al. (2002). Evidence for large decadal variability in the tropical mean radiative energy budget. *Science*, *295*(5556), 841–844. https://doi.org/10.1126/science.1065837

Wild, M. (2009). Global dimming and brightening: A review. *Journal of Geophysical Research*, *114*, 1–31. https://doi.org/10.1029/2008jd011470

Wild, M., Gilgen, H., Roesch, A., Ohmura, A., Long, C. N., Dutton, E. G., et al. (2005). From dimming to brightening: Decadal changes in solar radiation at Earth's surface. *Science*, *308*(5723), 847–850. https://doi.org/10.1126/science.1103215

Wild, M., Hakuba, M. Z., Folini, D., Dorig-Ott, P., Schar, C., Kato, S., & Long, C. (2018). The cloud-free global energy balance and inferred cloud radiative effects: An assessment based on direct observations and climate models. *Climate Dynamics*, *52*(7–8), 4787–4812. https://doi.org/10.1007/s00382-018-4413y

Wong, T., Wielicki, B. A., Lee, R. B., Smith, G. L., Bush, K. A., & Willis, J. K. (2006). Reexamination of the observed decadal variability of the Earth radiation budget using altitude-corrected ERBE/ERBS nonscanner WFOV data. *Journal of Climate*, *19*(16), 4028–4040. https://doi.org/10.1175/jcli3838.1

Young, A. H., Knapp, K. R., Inamdar, A., Hankins, W., & Rossow, W. B. (2018). The international satellite cloud climatology project H-series climate data record product. *Earth System Science Data*, *10*(1), 583–593. https://doi.org/10.5194/essd-10-583-2018

Zhang, Y., Rossow, W. B., & Stackhouse, P. W. (2006). Comparison of different global information sources used in surface radiative flux calculation: Radiative properties of the near-surface atmosphere. *Journal of Geophysical Research*, *111*(1–13), D13106. https://doi.org/10.1029/2005jd006873

Zhang, Y.-C. (2017). ISCCP-FH radiative flux profile produc, climate algorithm theoretical basis document (C-ATBD), NOAA NCEI climate data record (CDR) program, Retrieved from https://isccp.giss.nasa.gov/pub/flux-fh/docs/C-ATBD_ISCCP-FH.pdf, through login to Retrieved from https://isccp.giss.nasa.gov/projects/flux.html

Zhang, Y.-C., & Rossow, W. B. (1997). Estimating meridional energy transports by the atmospheric and oceanic general circulations using boundary fluxes. *Journal of Climate*, *10*(9), 2358–2373. https://doi.org/10.1175/1520-0442(1997)010<2358:emetbt>2.0.co;2

Zhang, Y.-C., Rossow, W. B., & Lacis, A. A. (1995). Calculation of surface and top of atmosphere radiative fluxes from physical quantities based on ISCCP datasets 1. Method and sensitivity to input data uncertainties. *Journal of Geophysical Research*, *100*(D1), 1149–1165. https://doi.org/10.1029/94jd02747

Zhang, Y.-C., Rossow, W. B., Lacis, A. A., Oinas, V., & Mishchenko, M. I. (2004). Calculation of radiative fluxes from the surface to top of atmosphere based on ISCCP and other global data sets: Refinements of the radiative transfer model and the input data. *Journal of Geophysical Research*, *109*(D19), D19105. https://doi.org/10.1029/2003jd004457

Zhang, Y.-C., Rossow, W. B., Long, C. N., & Dutton, E. G. (2010). Exploiting diurnal variations to evaluate the ISCCP-FD flux calculations and radiative-flux-analysis-processed surface observations from BSRN, ARM and SURFRAD. *Journal of Geophysical Research*, *115*(D15), D15105. https://doi.org/10.1029/2009jd012743

Zhang, Y.-C., Rossow, W. B., & Stackhouse, P. W. (2007). Comparison of different global information sources used in surface radiative flux calculation: Radiative properties of the surface. *Journal of Geophysical Research*, *112*(D1), D01102. https://doi.org/10.1029/2005jd007008